CFD4NRS-4, Conference on Experimental Validation and Application of CFD and CMFD Codes in Nuclear Reactor Technology, OECD/NEA and IAEA Workshop, 10.-12. September 2012, Daejeon, South Korea.

THE OECD/NEA MATIS-H BENCHMARK – CFD ANALYSIS OF WATER FLOW THROUGH A 5X5 ROD BUNDLE WITH SPACER GRIDS USING ANSYS FLUENT AND ANSYS CFX

Th. Frank[(1)], S. Jain[(2)], A.A. Matyushenko[(3)], A.V. Garbaruk[(3)]
[(1)]*ANSYS Germany GmbH, Staudenfeldweg 12, Otterfing, Germany*
[(2)]*ANSYS Inc.,* 10 Cavendish Court, *Lebanon, NH, USA*
[(3)]*New Technologies and Service (NTS), 27-a Gzhatskaya Street, St. Petersburg, Russia*
Thomas.Frank@ansys.com, http://www.ansys.com

Abstract
The OECD/NEA MATiS-H benchmark is based on experiments at the cold loop test facility at the Korea Atomic Energy Research Institute (KAERI), Daejeon, Korea. The MATiS-H test facility is used to perform hydraulic tests in a 5x5 rod bundle array at normal pressure and temperature conditions, with the aim of obtaining detailed experimental data for CFD turbulence model validation in a test configuration that resembles closely flow conditions in a real nuclear reactor fuel assembly with spacer grids. The test section consists of a 5x5 rod bundle array with a single spacer grid installed in a horizontal position.
The paper describes the applied CFD methodology for the detailed investigation of both types of spacer grid geometries – split type and swirl type – using the CFD software packages ANSYS CFX and ANSYS Fluent Vers. 14.0. Precursor CFD simulations have been carried out to obtain inlet flow profiles for fully developed turbulent flow in the 5x5 rod bundle and for a reduced subchannel geometry with periodic boundary conditions in the transverse directions in order to determine required mesh resolution, simulation time scale and numerical parameters for quality assurance of the final CFD solutions. ANSYS CFX and ANSYS Fluent results for the 5×5 rod bundle geometries applying the SST-CC, ω-based RSM as well as scale-resolving turbulence models SAS-SST and ZLES are finally compared to the experimental data of the MATiS-H benchmark.

1. INTRODUCTION

Computational Fluid Dynamics (CFD), already widely used in various branches of engineering, is gaining recognition as a potentially valuable tool for analyzing complex flow and heat transfer phenomena of relevance to nuclear plant safety. The use of CFD in the nuclear safety area is being promoted by international organizations. In April 2011, the Working Group on the Analysis and Management of Accidents (WGAMA) launched the "OECD/NEA Sponsored CFD Benchmark Exercise: Turbulent Flow in a Rod Bundle with Spacers" (OECD/NEA, 2011), based on the Korea Atomic Energy Research Institute (KAERI) MATiS-H[1] test facility (Chang, et al., 2008), (Kang, et al., 2010). This problem is topical, closely related to predicting subchannel flows in fuel bundles.
The subject of the initially blind benchmark exercise is the prediction of detailed velocity and turbulence distributions at different locations within a 5×5 rod bundle with two different types of vaned spacer grids (split and swirl type) under steady, single-phase, isothermal flow conditions. From a thermal hydraulic standpoint, predicting in fine detail the velocity and turbulence fields in a rod bundle is a challenging task. It requires the use of sufficiently fine numerical grids that represent exactly the geometrical specifications of the problem, with particularly high resolution near the guide vanes of the spacer grid where a substantial part of the turbulence and vorticity is being produced, and at the walls of the rods and the surrounding channel to capture the effect of boundary layers. Furthermore the accurate prediction of the strong swirling flow through the rod bundle downstream of the spacer grid requires the selection of appropriate turbulence models and least dissipative numerical schemes, where a compromise between accuracy (e.g. URANS) and computational requirements (e.g. LES) has to be found. In addition to the meshing and high-performance computing task, the CFD flow investigation of the rod bundle with the spacer grid is a challenge for application of the required level of CFD Best Practice Guidelines related investigations (Casey, et al., 2000), (Menter, 1998-2002),

[1] MATiS-H – Measurements & Analysis of Turbulence in Subchannels – Horizontal

(Mahaffy, 2010). Therefore we present in this paper the outline of the developed CFD investigation methodology, which has been started with CFD BPG related investigations on a smaller subset of the rod bundle geometry. Finally the experience gained and conclusions drawn from these precursor investigations have been applied to the investigation of the full MATiS-H benchmark geometries.

2. THE MATIS-H TEST FACILITY

A description of the experimental test facility of the cold loop MATiS-H test section at KAERI, Daejeon, Korea is provided in the OECD/NEA MATiS-H benchmark specification (OECD/NEA, 2011) in full detail. This test facility is aimed to perform hydraulic tests in a 5x5 rod bundle array in horizontal square sub-channel geometry at normal pressure and temperature conditions. Furthermore the aim is to study in detail the turbulent flow structures downstream of typical mixing devices as they are commonly used in fuel assemblies of nuclear reactors.
A schematic of the MATiS-H test facility is illustrated in Fig. 2.1. The main test section of the test facility shows a 170 x 170 mm^2 square channel which contains the 5x5 rod bundle array installed in a horizontal position. For fine-scale examination of the lateral flow structure on sub-channel geometry and for increased measurement resolution of the LDA measurements, the size of the 5x5 rod bundle array was enlarged 2.67 times from that of a real bundle and comprises 25 rods of 25.4 mm outer diameter in a regular matrix arrangement with a rod pitch P=33.12mm and a wall pitch of 18.76mm. Consequently, the hydraulic diameter of the channel cross-section, which considers the flow area and the wetted perimeter in a square duct including a 5x5 rod bundle, is D_H=24.27 mm.

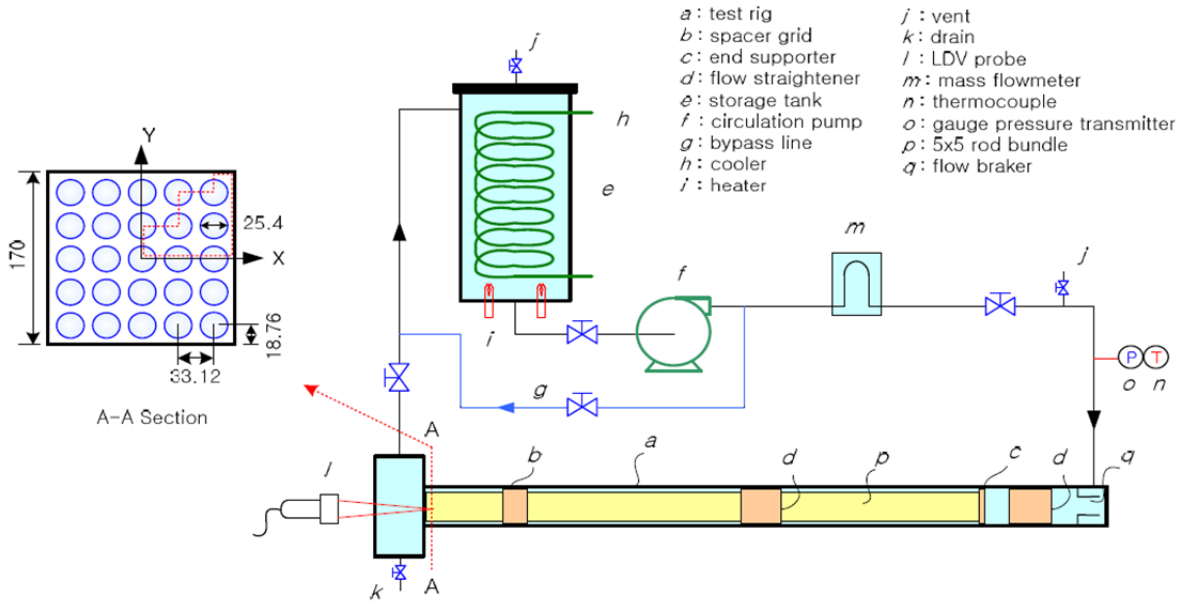

Figure 2.1: Schematic of the MATiS-H test facility at KAERI institute.

Water at 35°C at 156.9 kPa pressure is used as a working fluid for all the MATiS-H experiments. The mass flow rate in all experiments was 24.2 kg/s resulting in a bulk velocity of 1.5m/s corresponding to a Reynolds number based on the hydraulic diameter of Re=50250. All hydraulic and thermodynamic conditions of the test section were properly controlled during all tests. Furthermore extensive measures had been applied to provide fully controlled and fully developed flow conditions to the investigated spacer grids (b), Fig. 2.1. The water flow enters a lower plenum of the horizontal test section with an installed flow breaker. Then the flow passes two flow straighteners without guide vanes, which are installed to homogenize the flow and to accelerate the formation of fully developed flow profiles in the 5x5 rod bundle. The second of those flow straighteners (d) is installed at a distance of $100D_H$ upstream of the inlet cross-section of the spacer grid (b) under investigation. The developed flow profiles at $90D_H$ after that second flow straightener have been measured and were compared to CFD predictions for fully developed flow in the rod bundle (see section 5). From that it is assumed, that the rod bundle flow at the position $90D_H$ after the second spacer grid is fully developed, so that the further CFD

investigations can be limited to a section of the test facility comprising of a small length of rod bundle upstream of the investigated spacer grid (b) with fully developed inlet profiles, the split type or swirl type spacer grid (b) itself and again a section of the rod bundle of greater than $10.0D_H$ downstream of the tips of the spacer grid guide vanes to adequately include the measurement cross sections, thereby reducing the computational effort of the CFD investigations.
In the KAERI measurements at the MATiS-H test facility (Chang, et al., 2012), (Song, et al., 2012) a 2-D LDA device was installed in front of the main flow cross-section of the 5x5 rod bundle array for measuring the lateral velocity components on all the sub-channels. The axial velocity component was also measured by changing the position of the LDA probe to side measurements. In additional experiments it was checked, that the 120° symmetry flow in the outflow plenum on the left hand side of the test section has not disturbed the flow measurements at the measurement cross section A-A (Fig. 2.1) located 45mm upstream of the end of the rod bundle array and the outer square channel.
Two spacer grid types (b) were installed in the rod bundle array for detailed investigation. Both spacer grids have mixing devices and cause lateral mixing and/or swirling flow (see Fig. 2.2). The mixing devices used in this study were typical split-type and swirl-type, respectively. The spacer grids (b) can be moved in the axial direction along the 5x5 rod bundle array, in order to realize velocity measurements at different cross sections $0.5D_H$, $1.0D_H$, $4.0D_H$ to $10.0D_H$ downstream of the tips of the guide vanes of the spacer grids based on the test specifications, while the measurement cross section of the LDA device remaines in a fixed position. Further details of the measurements and the geometry of the investigated spacer grids can be found in the MATiS-H benchmark specifications (OECD/NEA, 2011). After the blind phase of the MATiS-H benchmark the velocity and turbulence measurements were provided for post-benchmark comparison with the CFD predictions.

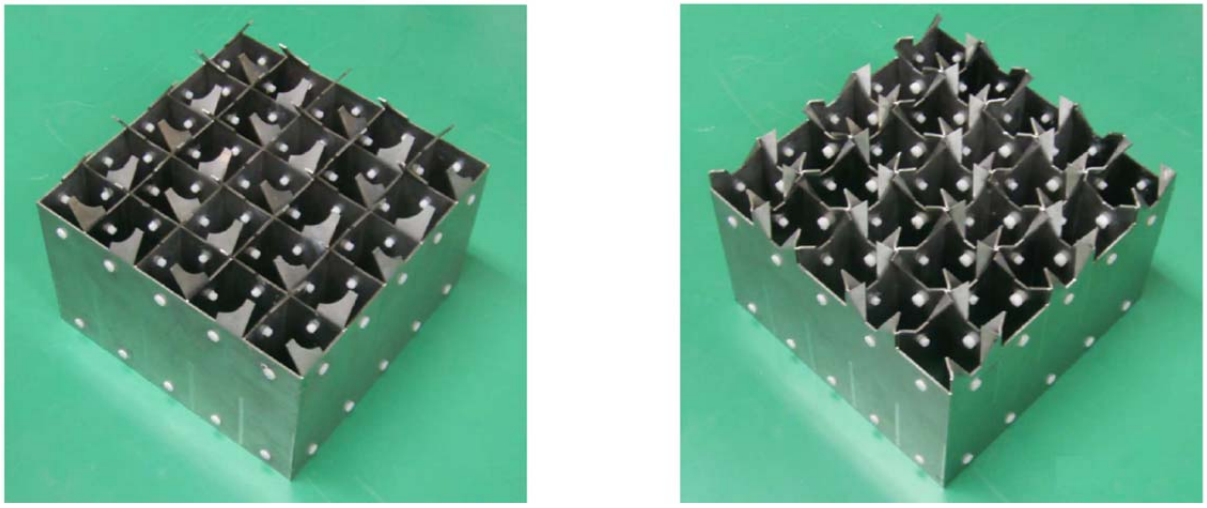

Figure 2.2. Test spacer grids used in the MATiS-H experiments; left: Split-type spacer grid; right: Swirl-type spacer grid.

3. RESULTING TEST MATRIX AND CFD SIMULATION METHODOLOGY

It was the aim of the CFD investigations for the MATiS-H benchmark to provide best possible CFD solutions for both types of spacer grids, using ANSYS CFX and ANSYS Fluent CFD software packages. For this goal it was a concern right from the beginning, that due to the level of detail and extent of the investigated flow geometries it would not be possible to apply CFD Best Practice Guidelines (Casey, et al., 2000) to their full extent to the full rod bundle geometries with spacer grids. Therefore it was decided to conduct precursor CFD simulations on geometries of reduced size. For these CFD BPG oriented studies the split-type spacer grid was selected. From the full 5x5 rod bundle geometry just one subchannel with the 4 adjacent rods was cut out and periodic boundary conditions were applied to the sides of the created subgeometry. Corresponding CFD investigations are discussed in section 4 of this paper. The reduction of the full rod bundle geometry to flow through one representative subchannel provided the advantage, that this reduced geometry allows required studies with respect to level of CFD solver convergence, mesh independence of the obtained solution and preliminary comparison of applied numerical discretization schemes and turbulence models.
A second series of CFD simulations were carried out to obtain fully developed flow profiles for the

5x5 rod bundle cross section (see section 5). These were used as inlet boundary conditions for the CFD investigation of the full benchmark geometry with the spacers. For this purpose a thin slice of the 5x5 rod bundle cross section with the outer square box was created and periodic boundary conditions with prescribed massflow rate of 24.2 kg/s were applied in the axial direction. The resulting fully developed flow profiles from SST with curvature correction (SST-CC) and ω-based RSM turbulence models are compared to the provided inlet flow profile measurements from the MATiS-H test facility (OECD/NEA, 2011).

Furthermore it became evident quickly, that the investigated spacer grid geometries introduce transient flow behavior within the spacer box, in regions downstream of the flow separation from the tips of the spacer guide vanes and in the large recirculation zones that are formed where spacer guide vanes are adjacent to the wall of the outer square channel. As shown in Fig. 4.2 two rows of fixation devices, so called buttons, are an important geometrical detail of the spacer design. Those cylindrical buttons are used to keep all the rods centered with respect to the grid of the spacer. The orientation of these buttons makes them classic cylinders in cross-flow and von Karman vortex shedding was observed even in preliminary CFD investigations, downstream of the two rows of distance elements, further interacting with the transient vortex shedding taking place at the guide vanes of the spacer grid. From that observation it became obvious, that despite the fact that the inlet flow conditions to the spacer grid are steady state and fully developed, the flow simulations for the full geometry would have to be carried out as transient, time-averaged CFD simulations with sufficient analysis flow time for full flow development and statistical averaging. The following cascade of CFD simulations has consequently been applied (see section 6 and 7):

1. Steady-state simulation on the coarsest mesh. Due to the inherent transient flow behavior this CFD simulation does not fully converge, but can be used as an improved initial guess for the following transient CFD simulation.
2. Initialization of the transient flow simulation from the steady-state solution allowing for enough time for flow development, which is characterized by appearance of regular patterns in monitored flow variables at several monitoring point locations downstream of the spacer grid.
3. For transient flow simulations on refined meshes the CFD simulation was initialized with the final result from the transient CFD simulation of the previous coarser grid level, again allowing for flow development time of 0.25s real time in order to eliminate possible errors in the CFD solution arising from mesh interpolation.

This results in the test matrix shown in Table 3.1 which has been applied to the MATiS-H benchmark investigations.

Flow geometry	**CFD solver**	**Meshes**	**Turbulence models**
Thin slice through 5x5 rod bundle with periodicity in axial direction	ANSYS CFX, ANSYS Fluent	Comparison of structured and unstructured meshes (ICEM-CFD, ANSYS Workbench Meshing)	SST-CC, BSLRSM or ω-RSM
Isolated subchannel of the split type spacer with transverse-periodic boundary conditions	ANSYS Fluent	4 levels of unstructured meshes (ANSYS Workbench Meshing)	SST-CC, ω-RSM, WMLES
Full geometry, split type spacer grid	ANSYS CFX, ANSYS Fluent	3 levels of unstructured meshes (ANSYS Workbench Meshing)	SST-CC, BSLRSM or ω-RSM, SAS-SST
Full geometry (with 180° periodicity), swirl type spacer grid	ANSYS CFX, ANSYS Fluent	2 levels of unstructured meshes (ANSYS Workbench Meshing)	SST-CC, BSLRSM, SAS-SST

Table 3.1: Test matrix of the CFD investigations for the MATiS-H benchmark exercise.

4. PRECURSOR SIMULATIONS FOR AN ISOLATED SUBCHANNEL FLOW

4.1. Geometry Simplifications

By studying the MATiS-H benchmark specification it is evident, that the scale of the benchmark geometry and the degree of geometrical detail is such, that it would be impractical to apply the standard investigations related to the CFD Best Practice Guidelines (Casey, et al., 2000) in their full extent to the full benchmark geometry of the 5x5 rod bundle with spacer grid. Therefore it was decided to carry out such investigations on required convergence levels of the CFD solution, grid independence of results and required mesh resolution, influence of discretization schemes and timescale of the transient solution on a simplified flow geometry. Fig. 4.1 shows how the simplified flow configuration for the CFD BPG oriented studies was derived from the full split type spacer configuration by cutting out one of the subchannels and by applying periodic boundary conditions to the resulting new flow boundaries in the diagonally opposite directions. With this approach all characteristic flow features are preserved and can now be studied at a much smaller expense in terms of overall mesh size, computational time and data volume to be handled during pre- and postprocessing. The computational effort for the study of flow phenomena and influence of numerical settings on CFD solutions in the reduced domain is about 12.5 times smaller than for the full benchmark geometry.

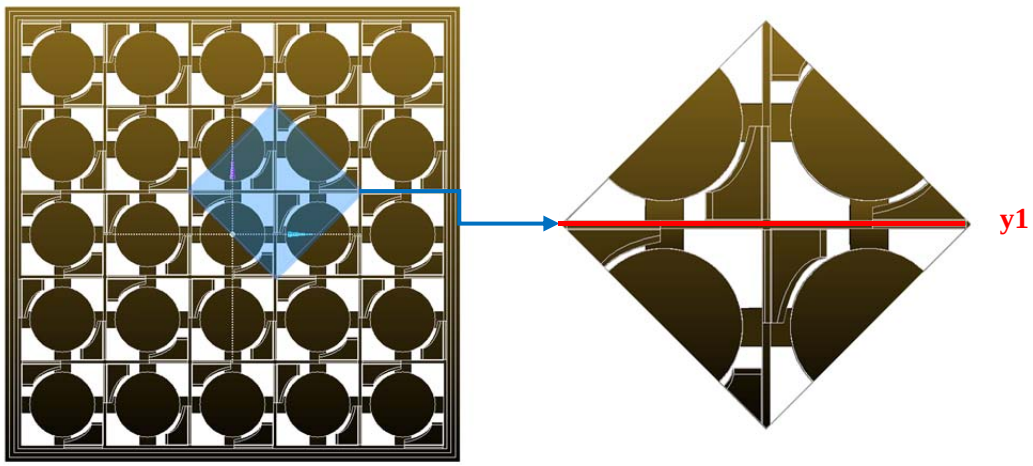

Figure 4.1: Full and periodic computational domains, split type spacer.

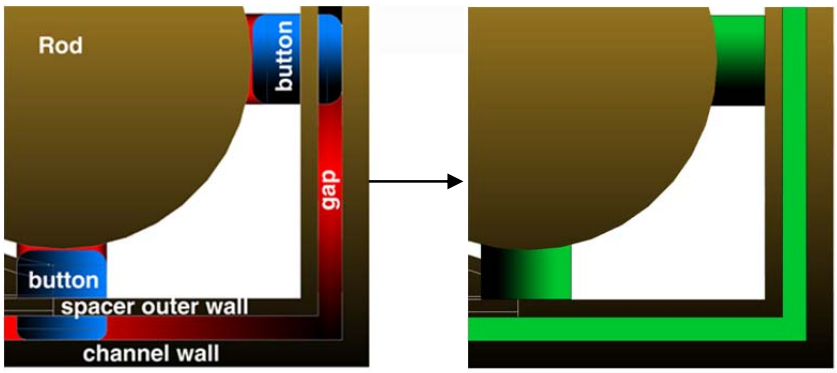

Figure 4.2: Original and computational model topology

Further, the original geometry provided by MATiS-H benchmark organizers includes two groups of small gaps. The first is a gap between rods and the so-called buttons – small cylinders used for spacer and rod fixation. The second is a gap between the outer limit of the spacer geometry and square channel walls. It was decided, that these gaps do not influence the flow results due to their small size, but would lead to significantly higher effort to resolve with a mesh. So it was decided to fill these small gaps by projecting the rounded buttons as solid cylinders flush with the rods (see Fig. 4.2).

Reynolds number based on the bulk velocity and the buttons diameter was predicted to be about 10^4, so unsteady flow around the cylindrical buttons in cross flow has to be anticipated. Preliminary computations showed that by using sufficient mesh and time resolution in the CFD simulation von Karman vortex shedding in the wake of the buttons could be observed (see Fig. 4.3). Further downstream those von Karman vortex streets are interacting with vortex shedding from the guide vanes of the spacer grid and thereby likely to affect the velocity and vorticity patterns at downstream cross sections where CFD results are to be compared with measurements. Consequently it was decided, that this type of flow has to be computed by transient, time-averaged URANS or perhaps by scale-resolving turbulence model approaches such as SAS-SST, DDES, ELES or WMLES

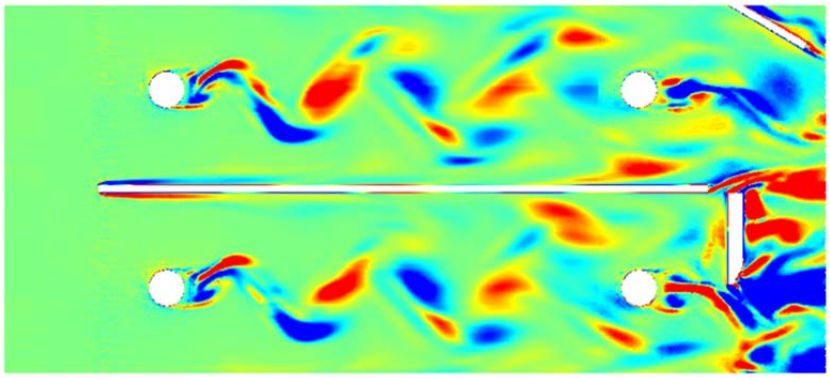

Figure 4.3: Von-Karman vortex shedding in button wake.

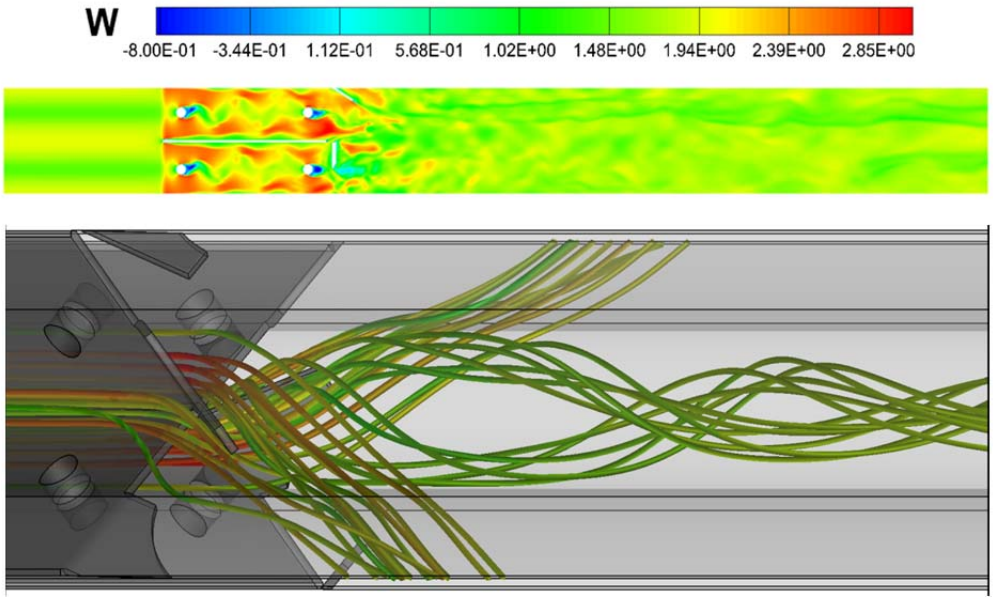

Figure 4.4: Flow structure visualized by axial velocity contours and streamlines.

Due to the complexity of the MATiS-H geometry and the flow around spacer grids, meshing requirements and computational parameters were a priory unknown. Therefore it was the primary aim for running the precursor simulations on the selected simplified domain with periodic boundary conditions to come up with recommendations for required mesh resolution and computational parameter settings for the following CFD investigations for the full benchmark geometry.

4.2. Periodic Domain – Details of CFD Investigations

All precursor simulations on the reduced periodic domain geometry were performed using ANSYS Fluent 14.0. As discussed in the previous section to capture the transient flow behavior a URANS approach was used for most computations. Water properties at 35°C were specified as a constant property incompressible liquid. Further two different models were chosen for turbulence closure of the set of governing equations. The first one is the well-known linear viscosity k-ω SST model. Since streamlines in the flow under consideration are significantly curved in strongly swirling flow

downstream of the spacer grid (Fig. 4.4) special curvature correction terms are taken into consideration (SST-CC model, (ANSYS Inc., 2011)). Even with the curvature correction terms the SST-CC turbulence model is still an isotropic turbulence model, which would not be able to predict secondary flows in cross section of a rod bundle which arises from wall friction on rod surfaces and anisotropic Reynolds stresses. Therefore as a second investigated turbulence model the omega-based Reynolds stress model (ω-RSM, (ANSYS Inc., 2011)) was selected.
Further a scale-resolving simulation (SRS) using the algebraic wall-modeled LES (WMLES) model was performed. This scale-resolving approach on a LES capable mesh resolution is significantly more accurate in terms of turbulence modeling, however computational requirements are much higher than URANS, mainly because of the required LES-type mesh and the restriction on Courant number for the selection of the computational time scale. The aim of this expensive comparison was to determine whether a URANS simulation would be sufficient for the capture of the main flow characteristics or whether a scale-resolving LES-type simulation would be required for this specific flow and geometry.

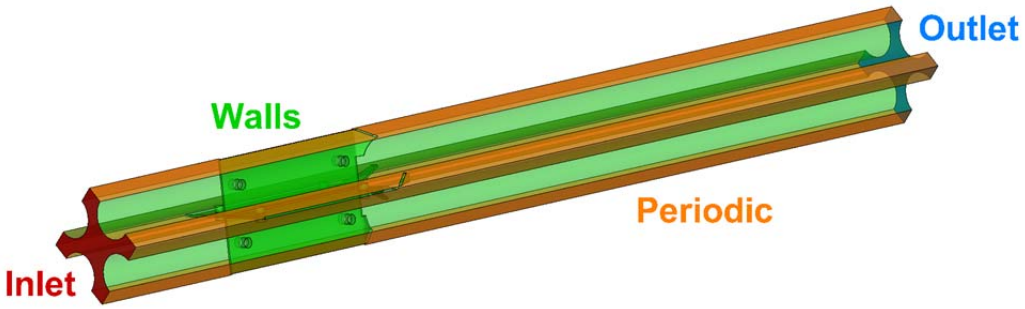

Figure 4.5: Topology of the computational domain and boundary conditions

Topology of the reduced periodic computational domain is shown in Fig. 4.5 together with applied boundary conditions. On the solid walls automatic near wall treatment was used. Constant static pressure level is specified on the outlet boundary and inlet boundary conditions depend on the approach used. Preliminary steady-state RANS simulations of fully developed flow were performed with both turbulence models, SST-CC and ω-RSM. Obtained velocity profiles and turbulent characteristics were used as inlet boundary conditions for the following URANS simulations. For the SRS method unsteady turbulent velocity profiles should be specified. Therefore the SST-CC fully developed velocity profiles in combination with the ANSYS Fluent vortex method (VM) were used.
Four different meshes were used for the URANS simulations (meshes 1-4 in Table 4.1). The first three meshes used the same topology and steps in the ANSYS Workbench Meshing process as was consequently applied to corresponding meshes used for CFD computations of the full MATiS-H benchmark geometry. So conclusions obtained from the CFD investigations for the reduced periodic domain are directly applicable as guidelines for the corresponding full benchmark geometry computations. The fourth mesh was specifically build for WMLES computations, so that it can be used for obtaining both URANS and SRS[2] solution. All the meshes were built taking into account the required mesh refinement parameters to resolve the specific flow details, namely the von-Karman vortex shedding after the rows of buttons and strong vortex structures appearing due to vortex shedding from the tips of guide vanes downstream of the spacer.

	Mesh 1	Mesh 2	Mesh 3	Mesh 4
Number of cells	1.6M	2.5M	7.6M	40M
Max. Y^+	17	13	8	5
Mean Y^+	7	5	3	1.5
Min cell size, mm	0.05	0.04	0.03	0.001
Max cell size, mm	2	2	2	1

Table 4.1: Parameters of different mesh levels for reduced periodic domain.

[2] SRS – Scale-resolving simulation

Grid requirements for SRS methods are significantly more stringent in comparison to URANS. In particular 10 mesh cells per boundary layer thickness should be provided in streamwise direction and 20 cells per boundary layer thickness in other directions. Mesh 4 as shown in Table 4.1 is the attempt to realize these meshing requirements for scale-resolving LES-like methods for this reduced periodic domain. From the resulting 40M mesh cells and the given reduction factor of 12.5 in comparison to the full benchmark geometry it became evident, that a scale-resolving WMLES simulation would become too expensive for the MATiS-H benchmark geometry and given computational resources.
With respect to the temporal resolution of the characteristic flow phenomena, one of the limiting criterions for the selection of the time step for the URANS computations is the necessity to resolve von Karman vortex street after the buttons in the spacer grid. Since the buttons represent cylinders in cross flow, the Strouhal number based on button diameter and streamwise velocity should be close to 0.2. For the time-accurate resolution of the flow around cylinders approx. 40 time steps per period are needed. This estimate results in a consideration for a suitable CFD time step of Δt=0.5 milliseconds.
For the SRS computation time step requirement results from the necessity to resolve the smallest turbulent structures. So the CFL number based on the streamwise grid resolution should be in the order of 1. For the given Mesh 4 (Table 4.1) the time step for the WMLES computations is determined to be as small as Δt=0.1 milliseconds.

4.3. Investigations on the Influence of Numerical Parameters

In order to provide independence of obtained URANS solution from computational parameters a few series of CFD computations and subsequent comparisons were performed. All the computations in this section were carried out using the SST-CC turbulence model. Furthermore the following discretization schemes were used: Green Gauss cell based gradient scheme and second order upwind scheme for pressure, momentum and turbulence characteristics. For higher accuracy the Green Gauss node based gradient scheme has been used in the final ANSYS Fluent computations for the full geometry.

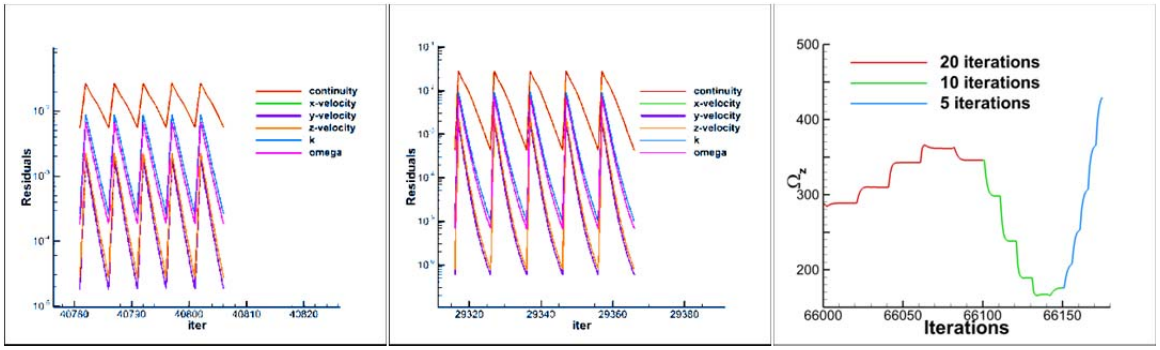

Figure 4.6: a, b : Convergence history for 5 , 10 iterations per time step;
c : Monitor plot of z vorticity at a point per iteration within time steps

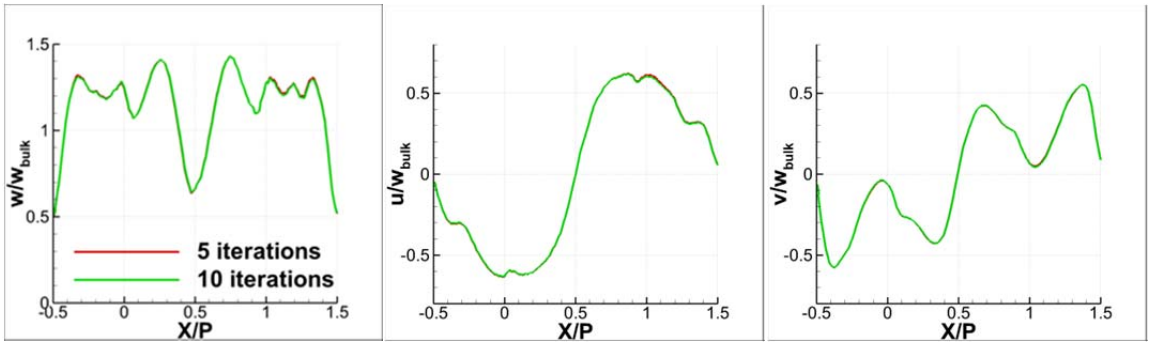

Figure 4.7: Influence of depth of convergence on the velocity profiles on line y1 at z = 0.5D_H

As a first step the required depth of convergence on each time step was investigated. The default settings in ANSYS Fluent requires a drop in solver residuals by 3 orders of magnitude indicating convergence In this investigation computations were performed by limiting the subiterations to 5 and

10 per time step to see if it was possible to save computational time. Convergence history is shown in Fig. 4.6 a, b and one can see residuals dropping steadily. It was observed that the time averaged velocity profiles shown in Fig. 4.7 are virtually the same. From this it can be concluded that further speedup can be achieved sometimes by limiting the number of iterations per time step. However when using this approach additional monitoring aids during the CFD solver run are recommended, such as the monitoring of solver imbalances and plotting of solved variables at key monitoring points over the subiterations per time step and ensuring the variables reach asymptotic levels within each time step. Such a monitor plot is shown in Fig 4.6 c for different number of iterations per time step.
The next significant parameter affecting the accuracy of the result of a URANS computation is the time duration for statistical averaging of results. For investigation two computations were performed at two different time samples, T=1 s real time corresponding to 50 von-Karman vortex street periods and T=2 s (100 periods). Results in Fig. 4.8 show that velocity profiles obtained with different duration of statistical averaging are very close to each other, so that it can be concluded that a time sample equal to T=1.0s can be used as a guideline for the MATiS-H benchmark computations resulting in sufficient accuracy of the statistical averaging procedure.

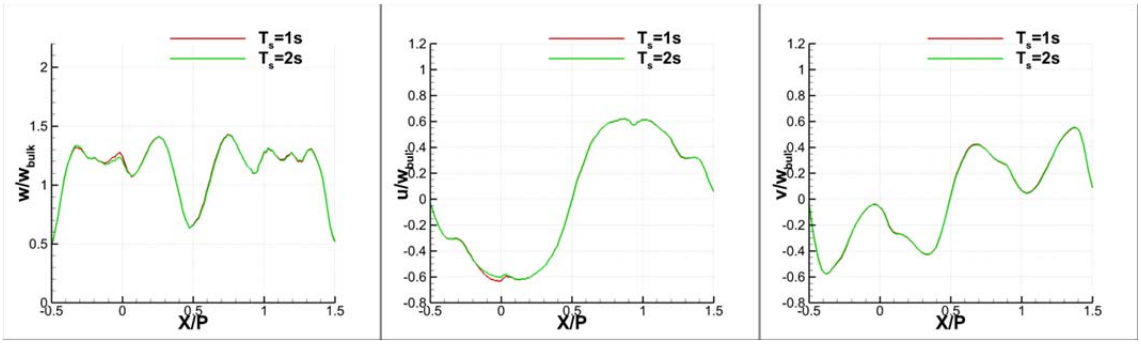

Figure 4.8: Influence of time sample of statistical averaging on the velocity profiles on y1 at z = 0.5D_H

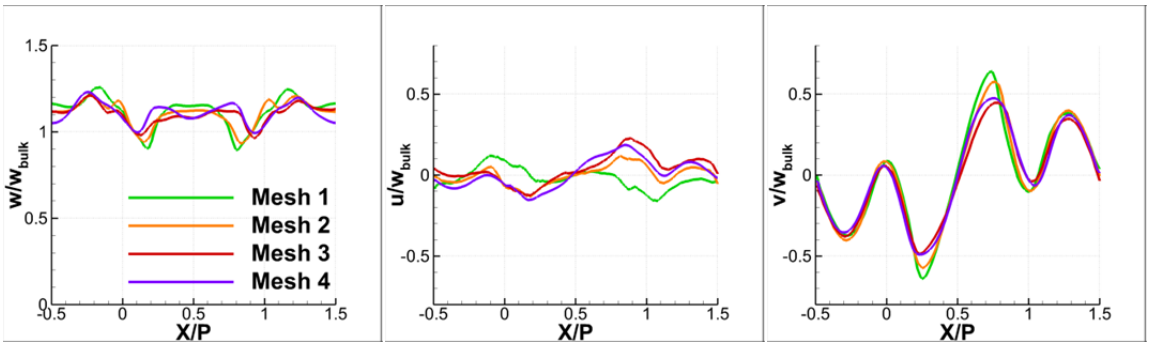

Fig. 4.9: Influence of mesh resolution on the velocity profiles on y1 at z = 4.0D_H

Finally the most significant question to answer for the MATiS-H benchmark investigations is the question for a sufficient spatial resolution of the used numerical meshes and whether mesh independent CFD solution can finally be obtained on the affordable mesh resolution. Computations were performed and results are shown in Fig. 4.9. Solutions for Mesh 3 and Mesh 4 were found to be quite close to each other so that Mesh 3 is sufficient to obtain mesh converged solutions for the URANS approach as applied to the full 5×5 rod bundle geometries.

4.4. Investigation of Turbulence Modeling Approaches

Further the different turbulence model approaches have been compared to each other. Fig. 4.10 and Fig. 4.11 show the comparison of the SST-CC and ω-RSM time-averaged URANS solutions on Mesh 3 for the z-component of the vorticity and velocity profiles at the measurement cross sections downstream of the spacer grid. URANS results are compared with the WMLES scale-resolving simulation on Mesh 4. As can be observed in the figures, the URANS and WMLES solutions are all quite similar looking. While on the one hand this lack of model sensitivity might indicate the flow is

being overly constrained by the reduced domain and applied periodic boundary conditions, on the other hand the relatively consistent URANS predictions justified using a URANS approach with both eddy viscosity turbulence models for the full 5x5 rod bundle geometry simulations as a first step and to meet the MATIS-H benchmark submission deadline

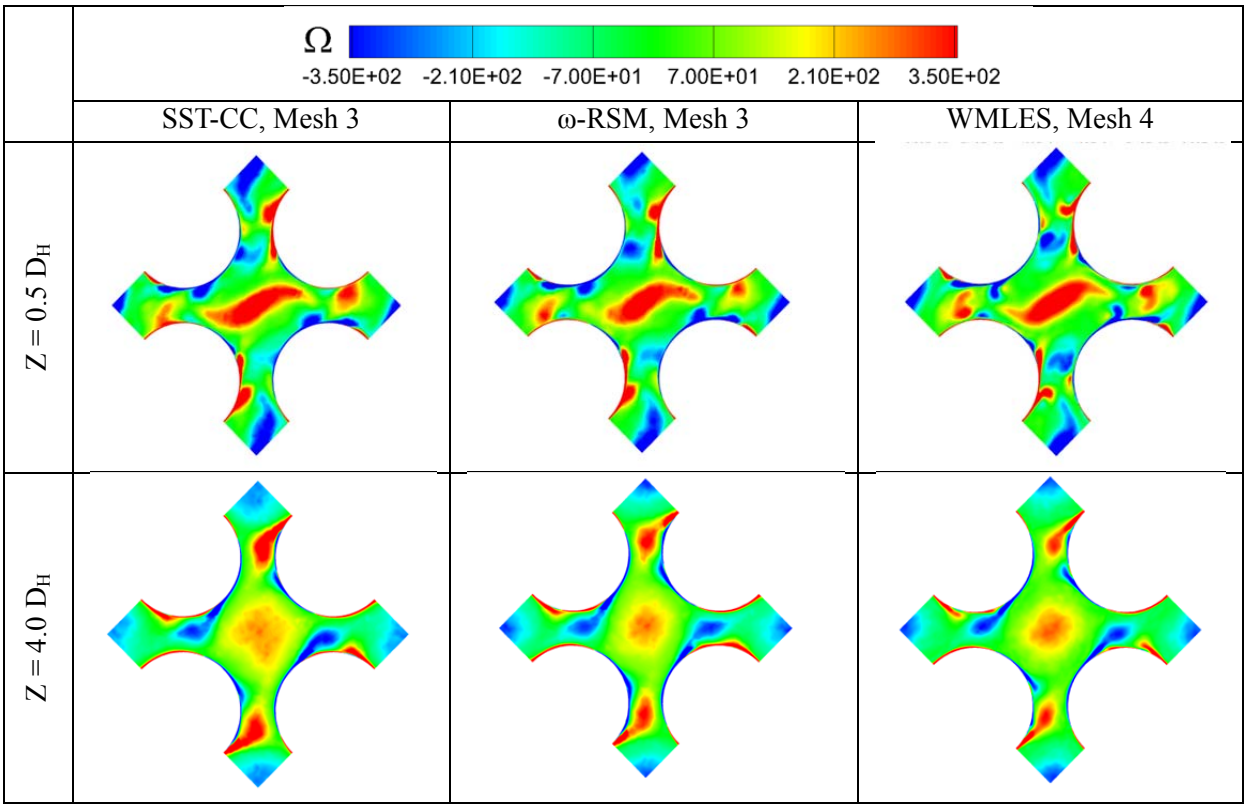

Fig. 4.10: Mean z-vorticity contours for different turbulence models

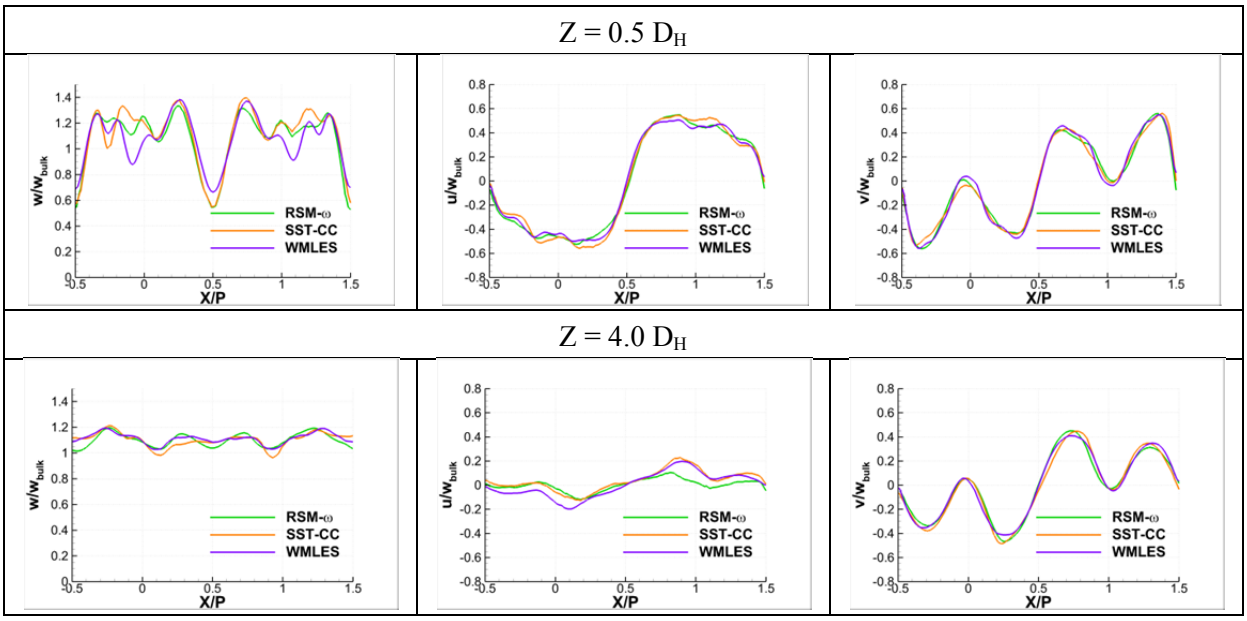

Fig. 4.11: Time-averaged velocity profiles for different turbulence models at different cross sections.

4.5. Conclusions from CFD Precursor Simulations

The following conclusions have been drawn from the CFD investigations on the isolated subchannel geometry with periodic boundary conditions applied in the transverse directions:

- Due to the observed transient flow behavior in the reduced subchannel geometry it would be desirable to use a scale-resolving LES-type simulation approach for the rod bundle geometry. However a full SRS simulation would require a mesh resolution similar to Mesh 4. For the full rod bundle a full WMLES simulation would result in an approx. 500 M elements mesh, which seemed infeasible with the available computational resources for the present study. As described in later section of this paper, simulations using SAS-SST[3] and ZLES SAS-SST[4], which are hybrid LES models, have been carried out for both spacer grid type geometries in post-test investigations.
- Nevertheless, resolution of the characteristic transient flow phenomena is required for an accurate CFD solution. The resolution of Mesh 3 with the identified meshing parameters for local mesh refinement should be used for the URANS computations on the full MATiS-H geometry. Developed monitoring approaches, guidelines for CFD solver convergence and sampling time have to be applied to the full geometry computations.
- SST-CC and ω-based RSM turbulence models have delivered in general quite similar solutions, which in turn were not substantially differing from the WMLES solution on Mesh 4. It cannot be excluded, that the periodic boundary conditions in x- and y-direction lead to additionally constrained fluid flow in the reduced domain which might differ from flow patterns in the full rod bundle. So from this investigation it is not obvious, if the URANS approach is adequate or which of the two compared URANS turbulence models is the better or more accurate approach. SST-CC is the less computational intensive approach, while the RSM turbulence models may have the advantage of anisotropy and the capability to predict the secondary flows in the cross section of the rod bundle leading to additional cross-sectional mixing. Therefore both turbulence models have been applied for the full 5×5 rod bundle geometry.

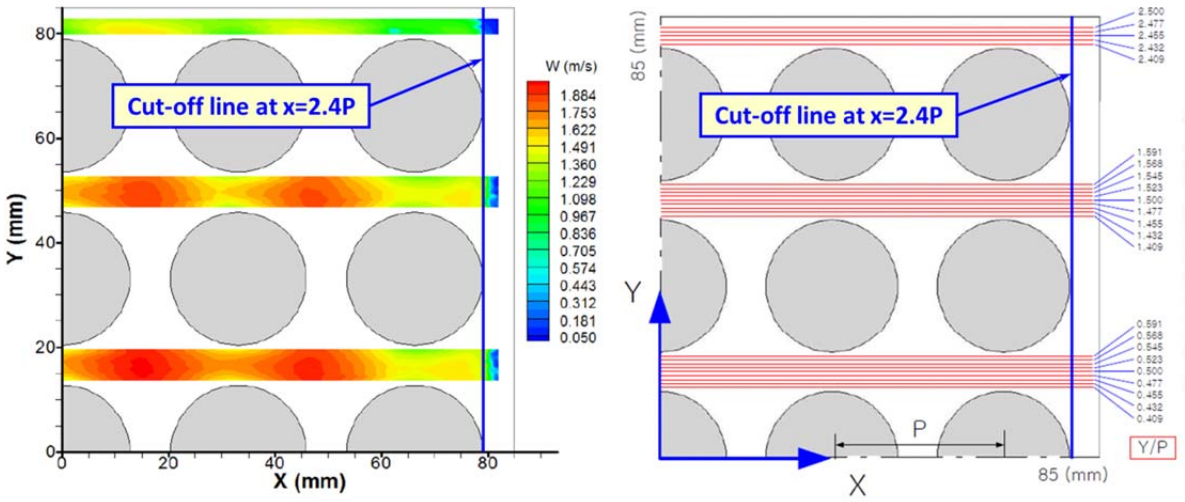

Figure 5.1: Measurements of fully developed rod bundle flow at 90DH downstream of the second flow straightener; measurement positions through subchannels of the rod bundle

5. VALIDATION OF INLET BOUNDARY CONDITIONS

In preparation of the MATiS-H benchmark specifications the KAERI institute had conducted a series of measurements with the aim of providing benchmark participants with inlet boundary condition data (OECD/NEA, 2011) for the intended CFD investigations of the two types of spacers. For this purpose the properties , , , and had been measured in narrow bands across subchannels in a cross section at $90D_H$ downstream of the second flow straightener (d) (see Fig. 2.1 and Fig. 5.1), which are intended to serve as inlet boundary conditions for the benchmark CFD investigations just upstream of the spacer (b). This data, while useful, can in practice be inconvenient to apply directly to CFD simulations sometimes. For example, a CFD simulation using a Reynolds stress model would require

[3] SAS – Scale-Adaptive Simulation
[4] ZLES – Zonal Large Eddy Simulation

the full set of all 6 independent Reynolds stress tensor components at the inlet cross section of the computational domain and the provided experimental data would be inadequate. Consequently it is necessary to conduct precursor simulations for fully developed flow in a 5x5 rod bundle in a square channel of 170x170mm^2. Such precursor CFD simulations can be carried out with the corresponding turbulence model used in the final MATiS-H benchmark investigation and thereby the exported fully developed cross sectional profiles of velocity components and turbulence properties can be directly used as inlet boundary conditions for the final runs. The provided experimental data can then be used for additional validation and solver comparison.
Such precursor CFD simulations for the derivation of fully developed 5x5 rod bundle flow can be carried out in ANSYS CFX and ANSYS Fluent inexpensively. For this purpose a transverse cut is made through the rod bundle geometry. This cross section is meshed in 2D and then extruded in the axial direction by a small distance. This creates a conformal mesh at the inlet and outlet boundary cross sections of that short length of the extruded rod bundle and periodic boundary conditions are specified with a target fluid mass flow rate of 24.2 kg/s. By doing that the geometry and flow represent fully developed flow conditions in an infinitely long rod bundle in a square channel. For the current investigation we created two different meshes using structured hexahedral meshing in ANSYS ICEM-CFD 14.0 and unstructured quad meshing with inflation layers in ANSYS Workbench Meshing 14.0. The resulting meshing parameters are of comparable mesh quality and are listed in Table 5.1. The resulting mesh resolutions around the corner rod of the bundle are shown in Fig. 5.2.

Meshing Parameter	**ANSYS ICEM-CFD Hexa**	**ANSYS Workbench Meshing**
Meshing type	Structured hexahedral, extruded	Unstructured quad with inflation layers, extruded
Extrusion depth, mm	25	1
Number of mesh elements	1.78 M	344.4k
Mesh elements in cross section	178.1k	114.8k
Mesh cells in axial direction	10	3
Minimum face angle	44°	33°
Max. element volume ratio	3.25	6.6
Max. Y+	2.5	2.6

Table 5.1: Meshing parameters for the z-periodic rod bundle geometry.

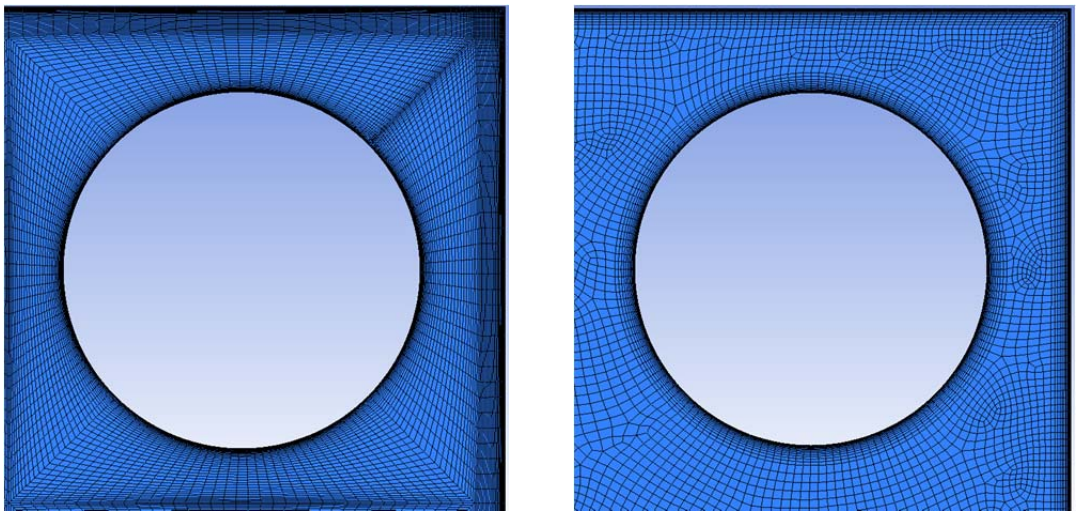

Figure 5.2: Mesh resolution around the corner rod of the bundle for the structured and unstructured meshes in z-periodic rod bundle geometry.

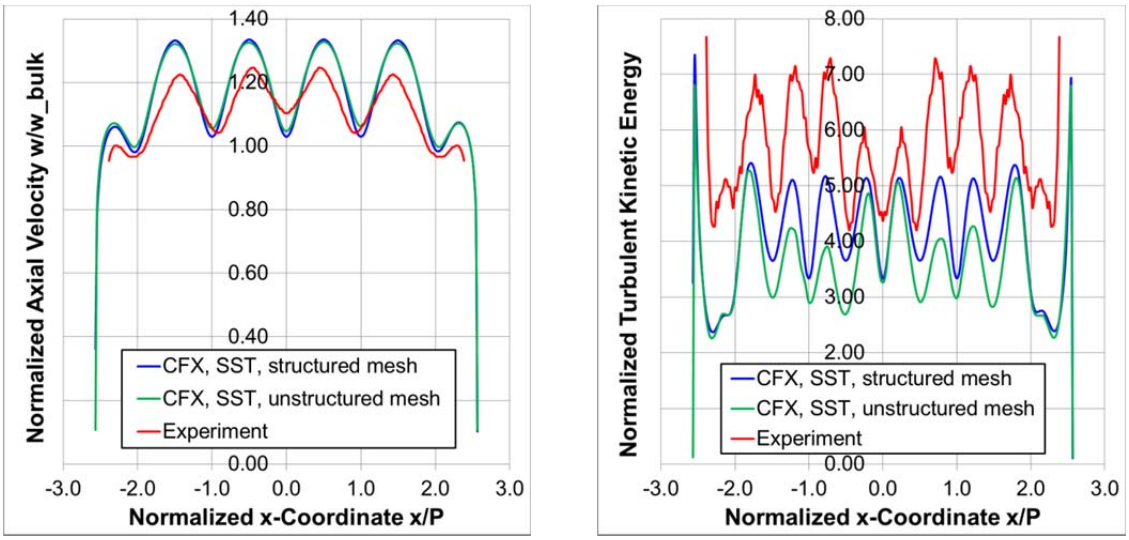

Figure 5.3: Comparison of ANSYS CFX SST turbulence model solution on structured and unstructured mesh, line y=1.5P.

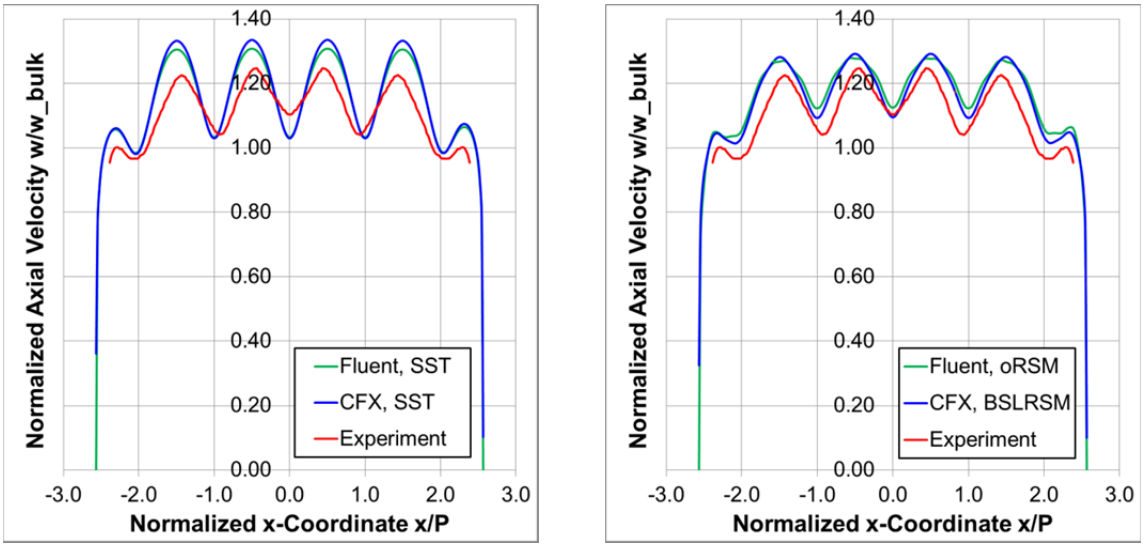

a) Normalized axial velocity component: SST and ω-based RSM models

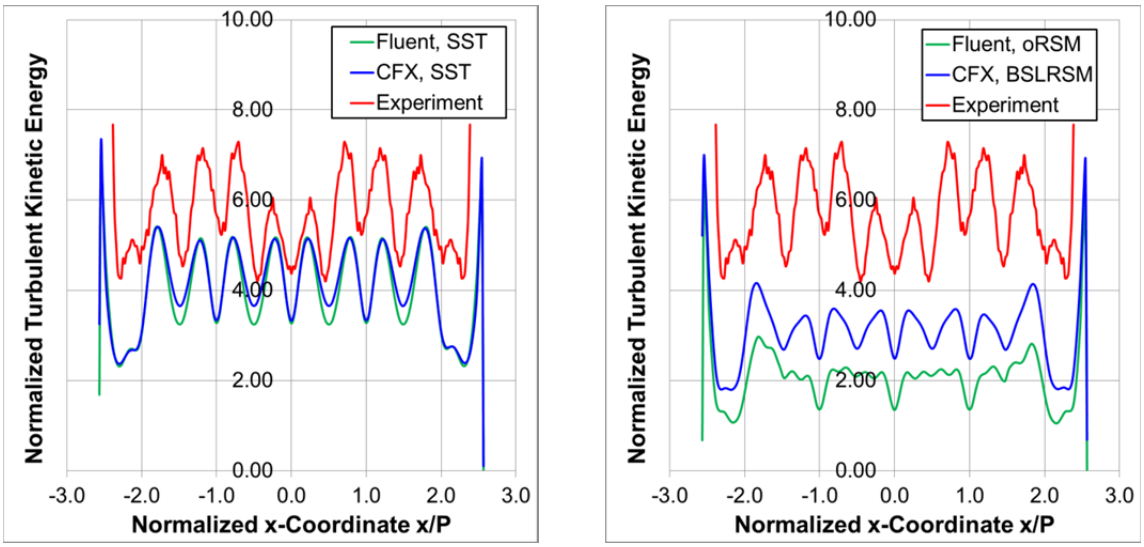

b) Normalized turbulent kinetic energy: SST and ω-based RSM models

Figure 5.4: Comparison of ANSYS CFX and ANSYS Fluent for SST and ω-based RSM turbulence model solutions on structured mesh, line y=1.5P.

Simulations were carried out on the two meshes, with ANSYS CFX using the SST and the BSLRSM model and with ANSYS Fluent using the SST and ω-RSM model (ANSYS Inc., 2011). In this flow configuration there is no strong swirl or streamline curvature, so the curvature correction terms in the SST model equations were not needed as it would not have any effect on the CFD solution. Calculations were performed in steady-state until a maximum residual of 10^{-5} and a conservation target of 10^{-4} had been reached.

Fig. 5.3 shows the comparison of the ANSYS CFX solution for the SST model on the structured and unstructured mesh in comparison to experimental data (OECD/NEA, 2011). Results are plotted in non-dimensional form along a line y=1.5P, where P is the rod pitch (P=33.12mm), $w_{norm} = w/w_{bulk}$ and $k_{norm} = k/w_{bulk}^2 \cdot 10^3$. Further communication with the KAERI experimentalists resulted in the clarification that the experimental data should be cut-off at the line x=±2.4P because the LDA measurement system was not able to obtain reliable data at distance any closer than that to the wall of the square channel (see position of the cut-off line in Fig. 5.1). The main reason for that is the finite elongation of the ellipsoidal shaped measurement volume of the LDA system, which at this distance begins to interfere with the channel walls, so that measured velocity and turbulent kinetic energy values are affected. The comparison of the mean axial velocity component, between the solutions on the structured and unstructured mesh do not show much difference. It is notable, that velocity maxima in the center of the subchannels are overpredicted by the SST model and that experimental data show a slight shift of those velocity maxima towards the center of the flow channel. Experimentalists from KAERI have explained this shift with the viscous effects from the outer channel walls, while in the CFD predictions such an effect has not been observed. For the turbulent kinetic energy the values are generally in good agreement, considering that the turbulence level in this flow is relatively low.

Fig. 5.4 shows the normalized axial velocity component w_{norm} and normalized turbulent kinetic energy k_{norm} compared between ANSYS CFX and ANSYS Fluent along the y=1.5P line. From this comparison it can be seen, that the Reynolds stress models show a substantially better agreement for the velocity profile, which is due to their anisotropic character and ability to capture secondary flows in the cross section of the rod bundle. The remaining small offset between the ω-based RSM model results and experiments are most likely explained by a slight difference in realized mass flow rate in the experiment in comparison to the specified one. For the turbulent kinetic energy profile the characteristic minima and maxima are found in the right locations, but the differences and the total level of turbulence are again relatively small so we abstain from discussion of the levels.

The outcome of these precursor CFD investigations was exporting fully developed flow velocity and turbulence property profiles which could be applied at the inlet cross section of the benchmark geometry. The comparison to data showed, that the ω-based RSM models seem to provide a slightly better agreement with data for the axial flow through the rod bundle. Further it could be shown that corresponding model formulations in ANSYS CFX and ANSYS Fluent gave almost identical results for the fully developed flow conditions.

6. THE 5X5 ROD BUNDLE FLOW WITH SPLIT TYPE SPACER

6.1. Geometry and Mesh Hierarchy

The geometry and mesh for the full benchmark geometry were created using the pre-processing software applications within the ANSYS Workbench platform, namely ANSYS Design Modeler and ANSYS Workbench meshing. The flow domain geometry was assembled in Design Modeler which is geometry modeling software with functionality for preparing simulation geometry including CAD interfaces, geometry creation and modification capabilities. The spacer grid geometry was supplied with the benchmark specification as CAD files in STP format. These were imported into ANSYS Design Modeler, minor CAD repair was applied to non-closed parts of the geometry and the surrounding flow geometry of the cylindrical rods and the outer square channel was created per the benchmark specifications. As explained previously a precursor simulation was done to obtain the developed flow profiles, so the CFD domain for the full benchmark geometry focused on the domain starting with fully developed inlet flow boundary conditions at 100mm upstream of the spacer grid box. The length of the spacer grid box is 103.1mm (119.9mm with vanes) and the rod bundle flow

section under investigation downstream of the spacer grid is 400mm (~ 16.5 D_H). The total length of the flow domain considered is 620 mm and is shown in Fig 6.1

Meshing is a crucial step in such an investigation. The mesh has to be adequate for the given turbulence model and should be of high quality. The generation of a structured hexahedral mesh (for e.g. in ANSYS ICEM-CFD) would have been preferred from a CFD accuracy point of view, but it was judged to be less flexible and too expensive to create such a mesh. Instead hybrid meshes were created using ANSYS Workbench meshing. The flow domain was decomposed into three bodies (a), (b), (c) as shown in Fig 6.1. The meshing strategy used was to create a tetrahedral mesh first in the middle section (b) and then to sweep resulting surface meshes in both directions in regions (a) and (c) with wedge elements to obtain a fully conformal hybrid mesh. In addition to global mesh controls, particular care was given to using controls on the mesh sizing on important flow obstructions such as the guide vanes, the spacer grid and the buttons. This is shown in the detail in Fig 6.2.The growth rate of the mesh from the surface mesh was controlled as well to ensure capturing the vortex structures generated downstream. Inflation layers were applied to all the wetted surfaces to adequately capture the boundary layers as required by the turbulence models. In this investigation all the turbulence models used an enhanced wall treatment which resolves the boundary layer and for which the recommended first cell height is Y^+~1. These models automatically blend to a wall modeled treatment depending on the value of Y^+. As can be seen from Table 6.1 the final mesh was within the acceptable order of magnitude range of Y^+ in the entire domain.

A mesh being in full compliance with all mesh generation rules set for a full LES-type SRS simulation and corresponding to Mesh 4 from Section 4.1 for the entire domain would be in the range of 500 M cells and would be prohibitive to perform a computation so that this task was not pursued during the blind phase of the MATiS-H benchmark. In post-test investigations Mesh3 was used for SAS-SST and ZLES simulations.

Table 6.1 shows the mesh hierarchy for the full benchmark geometry with the split type spacer grid corresponding to the hierarchy outlined in Section 4.1 for the periodic domain study.

	Mesh 1	**Mesh 2**	**Mesh 3**
Purpose of the mesh	CFD setup derivation	RANS/URANS tests	RANS/URANS productive mesh, SAS-SST & ZLES
Number of elements	11.0M	31.5M	96.3M
Number of nodes	4.4M	15.4M	40.6M
Y^+_{max} [5]	92.3	20.6	10.1
Y^+_{mean}	39.6	9.5	4.2
Min cell size, mm	0.1	0.04	0.03
Min face angle [°]	6.0	6.5	9.6
Growth rate	1.2	1.1	1.05

Table 6.1: Parameters of different mesh levels for the full benchmark geometry.

[5] ANSYS CFX and ANSYS Fluent use node centered vs. cell centered discretization schemes, which affects the definition of Y^+ and leads to different Y+ values for the same mesh. Here we specify the Y^+ values based on the ANSYS CFX simulation results. Due to the cell centered discretization of ANSYS Fluent corresponding Y^+ values on the same mesh are roughly by a factor of two smaller.

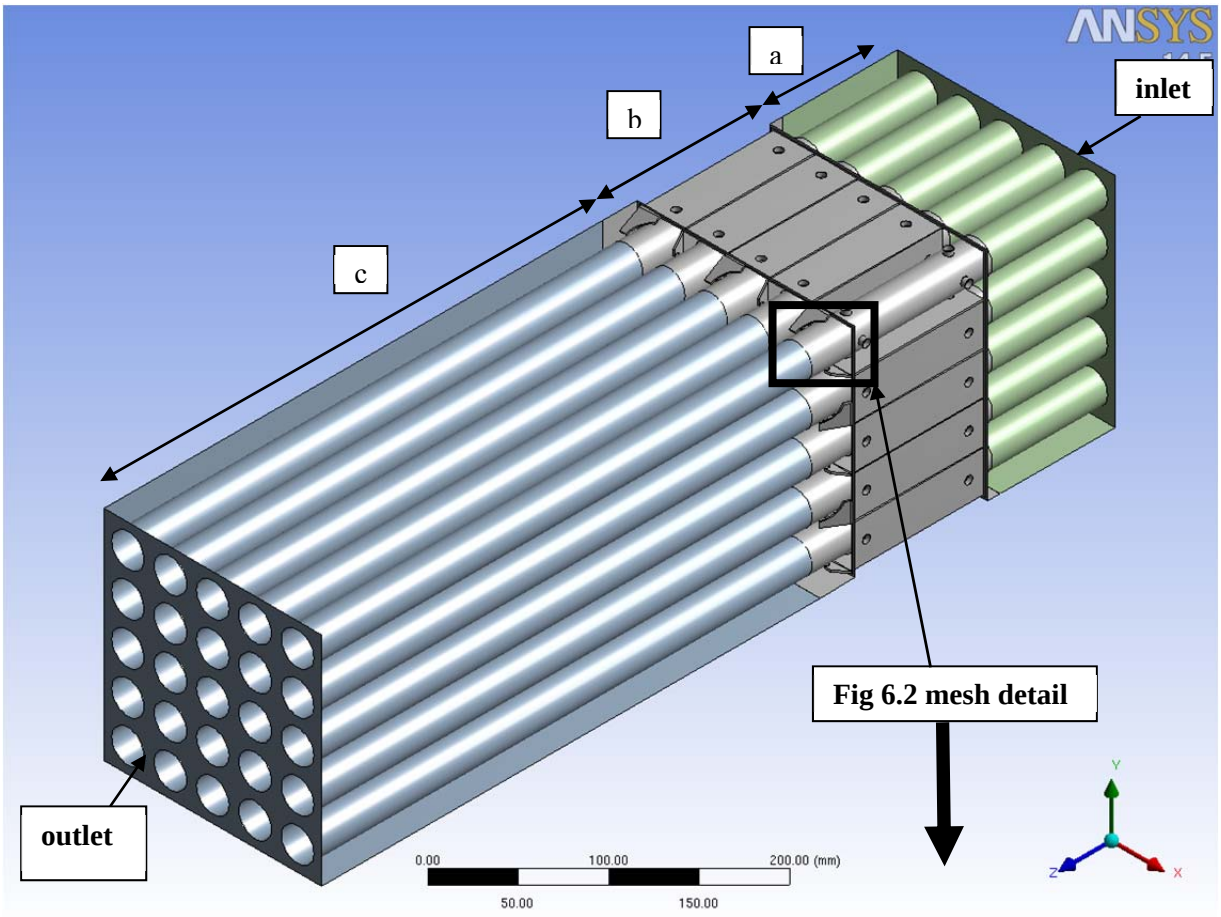

Figure 6.1: Computational Flow Domain. Inset showing zoomed mesh in Fig 6.2

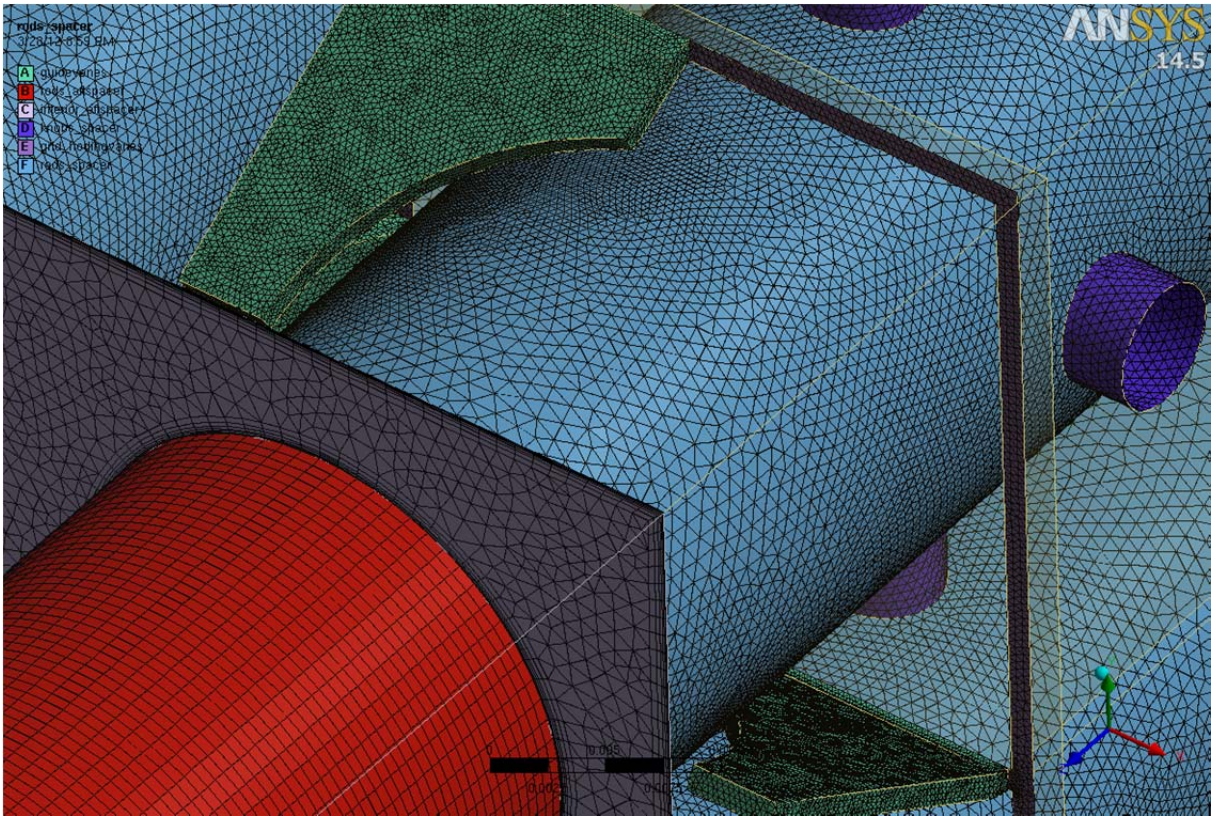

Figure 6.2: Hybrid mesh : Tetrahedral mesh in spacer to resolve guide vanes and buttons. Swept mesh on rods. Inflation layers on walls to resolve boundary layer.

6.2. CFD Test Matrix and Selected Turbulence Models

The CFD methodology applied in the investigation of the MATIS-H rod bundle geometry has already been outlined in section 3. Based on the investigations from section 4 the intended scope of the benchmark computations for the full rod bundle geometry included comparing ANSYS CFX and ANSYS Fluent using at least the SST turbulence model with curvature correction terms and the ω-based variants of the Reynolds stress turbulence models (BSLRSM and ω-RSM) (ANSYS Inc., 2011). From the precursor investigations for the reduced periodic geometry (see section 4) it was evident, that all simulations had to be carried out as transient, time-averaged URANS simulations. The solver settings used for both ANSYS CFD solver packages are given in Table 6.2 and the matrix of CFD simulations carried out for the split type spacer grid configuration is listed in Table 6.3.

Setup Option	ANSYS CFX	ANSYS Fluent
Turbulence Models	SST with curvature correction, Baseline RSM (BSLRSM)	SST with curvature correction, ω-RSM
Solver type	Coupled solver	SST-CC: Coupled solver ω-RSM: Segregated Solver
Advection scheme for momentum	HiRes	Second order upwind
Pressure discretization scheme	n/a	Second order
Advection scheme for turbulence	HiRes	SST-CC: Second order upwind ω-RSM: First order upwind
Gradient discretization	n/a	Green-Gauss node based (GGNB)
Transient scheme	2nd order backward-facing Euler	Second order implicit
Timestep initialization	Automatic	Previous timestep
Integration time step	0.0005s	0.0005s
Flow development time	0.25s	0.25s
Averaging time	1.25s (2500 samples)	1.0s (2000 samples)
Convergence criterion	RMS Res < $5 \cdot 10^{-5}$	Scaled Res < $1 \cdot 10^{-3}$
Max. number of coefficient loops / iterations	5 (for both SST-CC and BSLRSM)	10 for SST-CC 15 for ω-RSM
Inlet BC's	From corresponding precursor simulations on z-periodic thin rod bundle slice using the same turbulence model	
Domain initialization	Following outlined CFD methodology described in section 3	

Table 6.2: CFD setup for ANSYS CFX and ANSYS Fluent using SST-CC and ω-based RSM turbulence models.

ANSYS CFD solver	Turbulence model	Mesh 2	Mesh 3
ANSYS CFX 14.0	SST-CC	X	X
	BSL RSM	X	X
	ZLES SAS-SST[6]		X
ANSYS Fluent 14.0	SST-CC	X	X
	ω-RSM	X	X
	SAS-SST[6]		X

Table 6.3: CFD simulation matrix for the split type spacer grid configuration.

As discussed previously, the SST-CC and ω-based RSM turbulence model URANS simulations were run first to ensure meeting the benchmark submission deadline. However it was felt the transient

[6] ZLES SAS-SST and SAS-SST simulations have been carried out as post-test simulations after the blind phase of the MATiS-H benchmark.

characteristics could best be captured by SRS and it was of interest to compare URANS with SRS Therefore the scale-resolving simulations (SRS) on the finest available mesh were run to completion after the benchmark results deadline. For ANSYS CFX the Zonal LES approach was applied, where SAS-SST is applied as the SRS model in the full domain, but using a marker function for the zone with z>0.01m and applying the zonal LES approach the SAS-SST model is forced to switch to scale-resolving mode in the area beginning from the upstream edge of the spacer grid and further downstream of it. In ANSYS Fluent the SAS-SST approach has been applied without the explicit prescription of a zone for the SRS approach. Table 6.4 shows the solver settings used for both ANSYS CFD solver packages in SRS simulations for the split type spacer grid geometry.

Setup Option	ANSYS CFX	ANSYS Fluent
Turbulence Model	SAS-SST with Zonal LES	SAS-SST
Solver type	Coupled solver	Segregated solver
Advection scheme for momentum	Bounded CDS[7]	Split type: CDS Swirl type: Bounded CDS
Pressure discretization scheme	n/a	Second order
Gradient discretization	n/a	Split type: Green-Gauss Node Based Swirl type: Least Squares Cell Based
Transient scheme	2nd order backward-facing Euler	Bounded second order implicit
HOTR[8]	n/a	Split type: off Swirl type: on
Timestep initialization	Previous timestep	Previous timestep
Integration time step	0.00025s	0.0002s
Flow development time	0.25s	0.2s
Averaging time	1.0s (4000 samples)	Split type: 0.6s (3000 samples) Swirl type: 0.7s (3500 samples)
Convergence criterion	RMS Res < $1 \cdot 10^{-3}$	Scaled Res < $1 \cdot 10^{-3}$
Max. number of coefficient loops / iterations	5	Split type: 15 Swirl type: 7
Inlet BC's	From corresponding precursor simulations on z-periodic thin rod bundle slice using SST-CC turbulence model	
Domain initialization	From SST-CC URANS result on finest mesh	

Table 6.4: CFD setup for ANSYS CFX and ANSYS Fluent using SRS approach.

6.3. Obtained CFD Results and Comparison to Data

As mentioned all simulations in the blind phase of the MATiS-H benchmark were carried out as transient, time-averaged URANS simulations. This was done to capture the strong transient behavior of the flow downstream of the spacer and in order to limit at the same time the required computational effort to be able to apply a minimum of CFD best practice related investigations. From the preexamination in section 4 it is known, that there are three distinct transient phenomena occurring:

- The buttons in the spacer grid design for keeping the rods centered behave like cylinders in cross flow and cause von Karman vortex shedding.
- The guide vanes of the spacer grid show transient vortex shedding from their sharp edged tips and due to the recirculation zones behind them.
- Strong flow separation and large recirculation zones appear in the wake region formed by the guide vanes adjacent to the wall of the outer square channel.

Fig. 6.3 shows contour plots of the instantaneous axial velocity component w in yz-plane at the coordinate x=0.047m, which corresponds to a cutting plane through the middle of one row of buttons in the spacer grid. Since those images show instantaneous velocity distributions they are not directly comparable with each other in every detail, but the development of the von Karman vortex shedding

[7] CDS – Central differencing scheme
[8] HOTR – High order term relaxation

can be observed for all four different CFD simulations in each gap between the rods and the interior walls of the spacer grid. It should be noted that the spatial resolution of Mesh 2 was not sufficient in ANSYS CFX to resolve this von Karman vortex shedding, while the phenomenon was observed in the ANSYS Fluent simulations already on Mesh 2. Further a blue zone of negative w-velocities can be observed at the lower most guide vane on the right hand side of the spacer grid, which marks the large recirculation zone between this guide vane and the channel wall. Finally, from the different instantaneous realizations of the flow field it can be clearly seen, that the flow field is strongly transient in the region downstream from the spacer grid. Increased unsteadiness and finer structures are seen being resolved going from ANSYS Fluent to ANSYS CFX plots Figs 6.3 d to a.

Furthermore the guide vanes of the spacer grid introduce a complex pattern of strong vortices, which can be visualized and compared by plotting contours of the time-averaged z-component of the vorticity field ω_z. Fig. 6.4 and Fig. 6.5 show the comparison of the predicted z-vorticity patterns at two characteristic distances $z=0.5D_H$ and $z=4.0D_H$ downstream of the spacer grid, where the distance is measured from the tips of the guide vanes as specified by the MATiS-H benchmark specification (OECD/NEA, 2011). From Fig. 6.4 it can be seen, that immediately after the spacer grid a complex pattern of counter-rotating vortices of high z-vorticity amplitude exists. The observable vortex patterns are similarly predicted by both the SST-CC and the RSM turbulence models by both the ANSYS CFX and the ANSYS Fluent solutions. Here at $z=0.5D_H$ the URANS solutions do not substantially differ from the SRS approach solutions. The only remarkable differences at $z=0.5D_H$ exist in a slight change in shape and orientation of the main vortices in the centers of the subchannels of the rod bundle, where vortex structures appear slightly more elongated in the ANSYS Fluent solutions. At $z=4.0D_H$ and beyond it is observed that the vortices change their shape from the elongated vortices at z=0.5DH to almost round vortices (see Fig. 6.5). Here ANSYS CFX with the BSLRSM model are still showing clearly defined vortex structures and the SST-CC turbulence model solution obtained with ANSYS CFX solver shows only a slightly more dissipative character. The maximum amplitude of z-vorticity in the vortex cores is slightly less compared to the ANSYS CFX, BSLRSM solution. More turbulent vortex dissipation in this comparison of time-averaged vorticity is observable for the ANSYS Fluent, SST-CC and ω-RSM solutions. ANSYS Fluent URANS solutions show relatively smaller maximum z-vorticity amplitudes and the vortices are spread out over a wider area in the subchannels. This correlates inversely with the increased resolved velocity fluctuations observed in Fig 6.3 and 6.10 for the respective models.

Finally the ANSYS CFX and the ANSYS Fluent solution with SAS-SST scale-resolving turbulence model approaches show similarly reduced vorticity amplitude and a wider spread of the vortex structures over the subchannel cross sections. The explanation for this is that the URANS solutions tend to underpredict the strong transient turbulent fluctuations in this type of flow. Consequently the URANS solutions tend to predict more stationary locations of the vortex cores, and the resulting time-averaged vorticity patterns are less spread out and more clearly defined. On contrary the SAS-SST solutions resolve a wider range of turbulent length and time scales and predict stronger turbulent fluctuations of the vortex systems in the subchannels. This results in rapidly moving vortices over the cross section of the subchannels and consequently for the time averaging results in a more diffuse vortex pattern and reduced vorticity amplitude in the time-averaged solution. However this should not be confused with any numerical diffusivity of the CFD solvers.

Fig. 6.6 shows the location of defined line cross sections y1, y2 and y3 at different distances $z=0.5D_H$, $1.0D_H$, $4.0D_H$ and $10.0D_H$ downstream of the tips of the guide vanes of the split type spacer grid, which are used for the following quantitative comparison of time-averaged mean and RMS velocity component profiles. Further Fig. 6.7 shows the optical configuration at the KAERI MATiS-H test facility for front measurements (Chang, et al., 2012), (Song, et al., 2012). Due to the installed downstream end support for the 5×5 rod bundle shown in Fig. 6.7 a) the measurements for u- and v-velocity component and RMS values are limited to the shown sector of the rod bundle, see Fig. 6.7 c), where the support grid has been reduced to the possible minimum of flow path obstruction. Profiles for the axial w-velocity component and W_{RSM} values at lines y1, y2 and y3 are available from corresponding side measurements for the entire width of the rod bundle; see Fig. 6.7 b).

Figs. 6.8 a)-f) show the comparison of ANSYS CFX and ANSYS Fluent results obtained along line y2=49.68mm for $z=0.5D_H$, $z=1.0D_H$ and $z=4.0D_H$. Both solvers show similar if not equal results for the two compared URANS turbulence model approaches. Profiles of time-averaged z-component of velocity show that the results obtained with the SST turbulence model with curvature correction terms

deliver almost the same solution as the RSM turbulence models. Only some minor difference is seen, for example the predicted minima and maxima of axial velocity are slightly higher for the SST-CC model, which can be attributed to its isotropic character, which can miss the transverse secondary flows. Those are captured by the anisotropic RSM models which leads to redistribution of momentum in the transverse direction and therefore to a decrease in axial velocity extrema. When the URANS results were compared to the KAERI MATiS-H data it was found that characteristic velocity minima and maxima occur at the same x-coordinate, but essentially all the URANS simulations substantially overpredict these extrema in the axial velocity component profiles. The reason for this behavior of the URANS turbulence models is explained by the following two reasons:

1. By its derivation URANS is not able to resolve all relevant turbulent length and time scales of a turbulent flow and thereby underestimates the resolved turbulent fluctuations. A part of the turbulent fluctuations is modeled by the k equation and therefore for a fair direct comparison of U_{RMS} the amount of modeled and resolved turbulent fluctuations has to be summed together.
2. Further the observed strong vortex systems lead to high velocity gradients in the vortex cores and consequently to large eddy viscosity at the spatial location of the vortex structures/cores. In turn this might lead to a self-stabilizing effect in the URANS simulations, where the predicted vortex structures are more stationary in space than in reality. In the time-averaged profiles of velocity and vorticity components this leads to more sharply defined minima and maxima in comparison to SRS solutions and data, where the full cascade of turbulent eddies lead to broader smearing of those extrema due to fluctuation of the vortex structures in the open space of the rod bundle subchannels.

As previously outlined the SAS-SST scale-resolving turbulence model simulations were run to completion in the post-test phase of the MATiS-H benchmark using both ANSYS CFX and ANSYS Fluent on Mesh3. The results are exemplarily shown in Figs. 6.9 and 6.10 in comparison to data for line y1 at cross sections $z=0.5D_H$ and $z=4.0D_H$. For the time-averaged mean velocity component profiles the usage of SAS-SST in comparison to SST-CC model leads to some improvement in the predicted amplitudes of velocity extrema, but no significant changes can be observed in the general flow patterns. In contrast, from Fig. 6.10 it can be observed that not surprisingly the URANS turbulence model approaches (SST-CC) had underpredicted the RMS values of resolved velocity fluctuations, while the SAS-SST models in ANSYS CFX and ANSYS Fluent deliver quite a good agreement between predicted velocity RMS values and data, thereby showing that the SRS simulations resolve most of the turbulent fluctuations. Here it has to be mentioned again, that for a steady-state RANS solution the RMS values of resolved velocity fluctuations would be absolutely zero and that for a 1:1 comparison the amount of modeled turbulent fluctuations, i.e. the kinetic turbulent energy, would need to take into account for the comparison with measured RMS values of velocity fluctuations. The comparison in Fig. 6.10 shows only the resolved part of turbulent fluctuations for the CFD solutions. With increasing distance from the split type spacer grid the comparison with KAERI data seems to get even more accurate for the SRS solutions and the agreement between the SAS-SST solutions of the two ANSYS CFD solvers at $z=4.0D_H$ is very good as well. More detailed postprocessing shows, that similar good agreement between the SRS solutions and data can be obtained for lines y2 and y3 as well as for $z=10.0D_H$.

7. THE 5X5 ROD BUNDLE FLOW WITH SWIRL TYPE SPACER

7.1. Geometry and Mesh Hierarchy

The geometry and mesh creation for the full benchmark geometry with the swirl type spacer grid (see Fig. 2.2) followed essentially the same steps as described in paragraph 6.1. The swirl type spacer geometry shows a 180 degree periodicity and a 90 degree symmetry, so that in principle it would be possible to simulate just 1/4th of the full geometry. But if 90 degree symmetry resulting in 1/4th of the full geometry would be assumed, then the symmetry planes x=0 and y=0 would cut rows of cylindrical buttons at in half and the imposed symmetry boundary conditions, would suppress the van Karman vortex streets shedding which would disturb the development of transient flow downstream of these cylindrical buttons in the spacer geometry. A 180 degree half periodic domain also cuts the buttons but the periodic boundaries allow the development of transient vortices across them. Also any potential

interference with the lines of data comparison at y1, y2 and y3 is avoided. Therefor for this benchmark exercise it was finally decided to make use of the 180 degree periodicity and to simulate half of the geometry (see Fig. 7.1).
Furthermore the 5×5 rod bundle geometry with swirl type spacer was decomposed in three parts: (b) the spacer grid including the rows of buttons and attached guide vanes, (a) the 5×5 rod bundle geometry from the inlet cross section up to the entry cross section into the spacer and (c) the 5×5 rod bundle geometry downstream of the spacer. As described in paragraph 6.1 for the split type spacer grid geometry the mesh for the part (b) was generated as a tet/prism mesh using ANSYS Workbench Meshing 14.0. Next the resulting surface meshes at interfaces with parts (a) and (c) have been extruded along the axial coordinate of the rod bundle, resulting in hexahedral boundary layer mesh around the rods of the rod bundle and prism mesh in the core of the subchannels. All mesh interfaces were created as fully conformal hybrid mesh including matching mesh interfaces for the periodic boundary conditions at y=0 (Fig. 7.1).
The resulting Mesh 2 for the 180 degree periodic domain had 108.7 M mesh elements, 40.6 M nodes, Y^+_{mean} = 2.3 and a Y^+_{max} = 5.9 (based on the vertex centered discretization of ANSYS CFX, see remark in paragraph 6.1). Thus the created numerical mesh exceeds the mesh resolution of Mesh 3 for the split type spacer geometry and shows the same high quality for other mesh metrics.

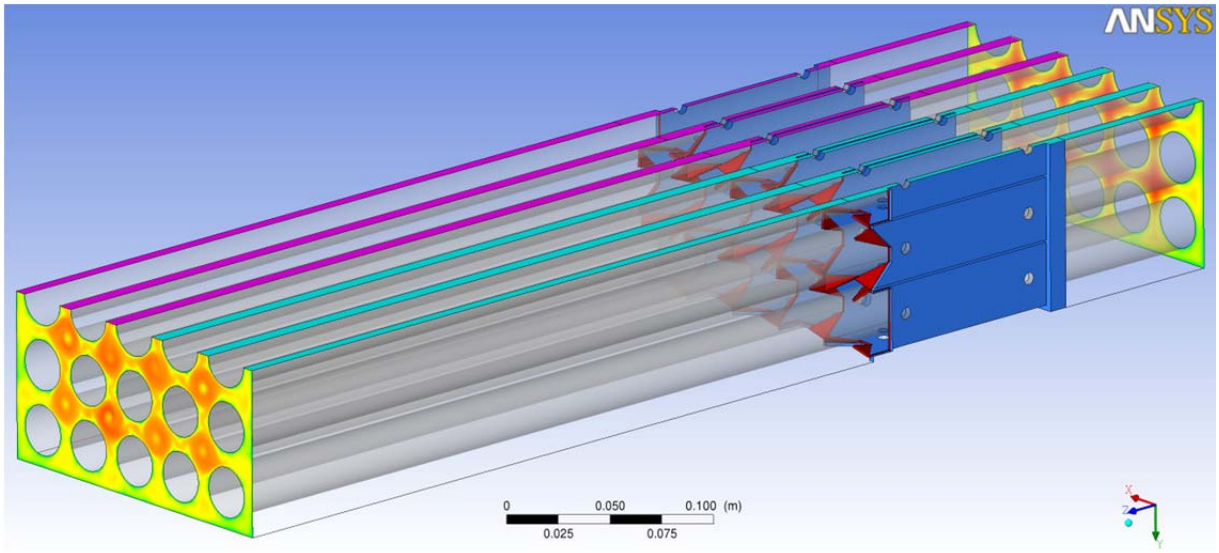

Figure 7.1: Computational domain of swirl type spacer grid geometry. Magenta and cyan surfaces are connected with periodic boundary conditions using conformal mesh.

7.2. CFD Test Matrix and Selected Turbulence Models

For the URANS simulations with the swirl type spacer grid there was time to run only one turbulence model for each solver so it was decided to run the simulations for the 180 degree periodic swirl type spacer geometry with BSLRSM model in ANSYS CFX and with the SST-CC model using ANSYS Fluent. Again simulations had been carried out as transient, time-averaged URANS simulations using essentially the same numerical parameters as specified in Table 6.2. The maximum number of coefficient loops/iteration had to be increased to 15 for the BSLRSM model in ANSYS CFX, and as the simulation progressed in time only 7-10 coefficient loops were used to reach the convergence criterion. For the ANSYS Fluent SST-CC simulation the gradient discretization method was set to Least Square Cell Based.
As for the split type spacer grid geometry SAS-SST (ANSYS Fluent) and ZLES SAS-SST (ANSYS CFX) scale-resolving turbulence model approach simulations had been carried out in the post-test phase of the MATiS-H benchmark, using the available Mesh 2.

7.3. Obtained CFD Results and Comparison to Data

The CFD simulations for the swirl type geometry essentially showed the same transient flow patterns as discussed in paragraph 6.3, with the difference that the different design of the swirl type spacer grid induces strong counter-rotating vortices in each subchannel. Flow patterns are visualized in Fig. 7.2

for both types of spacer grids and it can be observed, that the split type spacer leads to a redistribution and flow mixing between subchannels, while the swirl type spacer grid leads to one dominating vortex per subchannel.
This flow pattern can be seen from the Fig. 7.3 as well, where contours of time-averaged z-component of vorticity at xy-plane cross sections at $z=0.5D_H$, $z=1.0D_H$, and $z=4.0D_H$ downstream of the swirl type spacer grid are shown. From the images again it can be observed, that the ANSYS CFX solution applying BSLRSM model leads to higher vorticity amplitude at larger distance from the spacer grid in comparison with the ANSYS Fluent SST-CC solution. The differences in the CFD solutions are caused by differences in the applied turbulence models as well as by the prediction of larger flow field fluctuations and smaller turbulent length and time scales by the ANSYS Fluent solver leading to the dispersion of the vortex cores over a larger area in the time-averaged solution.
Fig. 7.5 shows the time-averaged axial velocity component w at lines y1=16.56mm and y3=81.29mm for axial distances of $z=0.5D_H$, $z=1.0D_H$ and $z=4.0D_H$ from the spacer vanes tip, for the ANSYS CFX and ANSYS Fluent URANS solutions in comparison to the data from the KAERI MATiS-H test facility (Chang, et al., 2012). The same observation as for the split type spacer grid geometry can be made, that the URANS solutions are predicting the cores of the spacer grid induced vortices in the right locations but tend to substantially overpredict the minima and maxima in the velocity profiles. Furthermore the strong swirling flow in the subchannels is preserved for too long a distance downstream of the spacer grid, which is caused mainly by the underprediction of turbulent fluctuations and the inherent limitation of URANS in the resolution of turbulent length and time scales. Nevertheless it can be mentioned, that the ANSYS Fluent and ANSYS CFX URANS solutions are similar.
Post-test calculations have been carried out for the swirl type spacer grid geometry on Mesh2 using the SAS-SST ZLES (ANSYS CFX) and SAS-SST (ANSYS Fluent) scale-resolving turbulence model approaches. Model parameter settings for these post-test simulations are summarized in Table 6.4. The SRS simulations have been carried out on the half geometry with the same periodic boundary conditions for the 180 degree rotational symmetry as applied for the URANS simulations.
Fig. 7.4 shows the comparison of the resulting SAS-SST results for contours of time-averaged z-component of vorticity at xy-plane cross sections at $z=0.5D_H$, $z=1.0D_H$, and $z=4.0D_H$ downstream of the swirl type spacer grid. Here the scale-resolving turbulence model approach solutions of both solvers ANSYS Fluent and ANSYS CFX are in almost perfect agreement. At $z=4.0D_H$ both solvers predict lesser time-averaged z-vorticity in comparison to the URANS solutions due to the non-stationary behavior of the vortices in the subchannels and possible vortex breakdown by turbulent fluctuations.
Finally Figs. 7.6 and 7.7 show comparison of the SAS-SST results from both ANSYS CFD solvers with data for line y1 at cross sections $z=0.5D_H$ and $z=4.0D_H$. The time-averaged v-velocity component is in very good agreement with data. The time-averaged axial w-velocity component is in fairly good agreement to data with slight overprediction of velocity extrema at $z=0.5D_H$ and a slight general overprediction of velocity level at $z=4.0D_H$, where the latter might be attributed to slight variations in mass flow rate in the experiment from the nominal value or to slightly different distribution of mass flow over different rows of subchannels in the rod bundle. The comparison of time-averaged u-velocity profiles at $z=0.5D_H$ with data shows some anomalies. While the CFD results show symmetric profiles with respect to the center location of subchannels with alternating positive and negative u-velocities on both sides of a vortex core, the measurements show all positive values of u-velocities for almost the entire y1 cross section on both distances from the spacer, which is rather unlikely and measurement errors on the general small velocity amplitude for this velocity component might play a role here.
Fig. 7.7 shows the comparison for RMS values of velocity fluctuations at $z=0.5D_H$ and $z=4.0D_H$. The SAS-SST results show the correct amplitude of turbulent fluctuations directly after the swirl type spacer grid. At larger distance at $z=4.0D_H$ the RMS values of velocity fluctuations from both CFD solutions are in nearly perfect agreement with the data. Again the ANSYS Fluent and ANSYS CFX solutions for the SAS-SST model approach on identical numerical meshes compare well with each other.

8. SUMMARY & CONCLUSIONS

The single-phase turbulent water flow through a 5x5 rod bundle array installed in a horizontal position and with split type and swirl type spacer grids has been investigated in accordance with the OECD/NEA MATiS-H benchmark specifications (OECD/NEA, 2011) using ANSYS CFX and ANSYS Fluent 14.0. Flow predictions have been carried out using the SST turbulence model with curvature correction terms, ω-based RSM turbulence models as well as WMLES and SAS-SST scale-resolving turbulence model approaches.

The paper describes the established CFD investigation methodology which allows the application of major principles of ERCOFTAC CFD Best Practice Guidelines (Casey, et al., 2000), (Menter, 1998-2002) to this rather complex application. From the investigations it has been demonstrated, that the flow through the spacer grids and rod bundle shows an inherent strong transient behaviour and therefore all CFD computations have to be carried out at least as time-averaged URANS simulations, but preferably using scale-resolving turbulence model approaches like SAS-SST. The required mesh resolution, numerical parameters and fully developed flow inlet boundary conditions were derived from precursor CFD simulations.

The finally obtained CFD solutions for the full MATiS-H benchmark geometry with spacer grids are in general good agreement between the two ANSYS CFD software packages (ANSYS CFX and ANSYS Fluent) and between the SST-CC, ω-based RSM and SAS-SST turbulence models. The qualitative patterns of vorticity are observed to be the same but it was found, that the URANS approaches tend to underpredict the turbulent fluctuations of spacer grid induced vortex structures in space and time which leads to an overprediction in velocity and vorticity extrema in the investigated line profiles in comparison to measurements. Finally scale-resolving simulations applying the SAS-SST model on the finest available meshes have led to very good agreement between ANSYS CFD solutions and the KAERI MATiS-H benchmark data for both types of spacer grid geometries (Chang, et al., 2012). The SAS-SST solutions not only show a more accurate prediction of mean velocity components, but are obviously as expected able to predict enhanced turbulent mixing in the rod bundle subchannels and RMS values of velocity fluctuations in substantially better agreement to data then the investigated URANS approaches.

9. ACKNOWLEDGEMENTS

SPONSORED BY THE
Federal Ministry of Education and Research

This research has been supported by the German Ministry of Education and Research (BMBF, Grant No. 02NUK010G) in the framework of the R&D funding concept of BMBF "Basic Research Energy 2020+", the German CFD Network on Nuclear Reactor Safety Research and the Alliance for Competence in Nuclear Technology, Germany.

REFERENCES

ANSYS Inc. 2011. *ANSYS CFX 14.0 Solver Theory Guide.* s.l. : ANSYS Inc., Canonsburg, USA, 2011.

—. 2011. *ANSYS Fluent 14.0 Theory Guide.* s.l. : ANSYS Inc., Canonsburg, USA, 2011.

Casey, M. and Wintergerst, T. 2000. *Quality and trust in industrial CFD – best practice guidelines.* s.l. : ERCOFTAC Special Interest Group on "Quality and Trust in Industrial CFD", Sulzer Innotec, Fluid Dynamics Laboratory, 2000.

Chang, S. K., et al. 2008. Phenomenological investigations on the turbulent flow structures in a rod bundle array with mixing devices. *Nucl. Eng. Design, Vol. 238.* 2008, pp. 600-609.

Chang, S.-K., Kim, S. and Song, C.-H. 2012. *OECD/NEA-MATiS-H Rod Bundle CFD Benchmark Exercise Test.* s.l. : CFD4NRS-4, Conference on Experimental Validation and Application of CFD and CMFD Codes in Nuclear Reactor Technology, OECD/NEA and IAEA Workshop, 10.-12. September 2012, Daejeon, South Korea, 2012.

Kang, H. S., Chang, S. K. and Song, C.-H. 2010. *CFD analysis of the MATiS-H experiments on the turbulent flow structures in a 5x5 rod bundle with mixing devices, Proc. CFD4NRS-3, Washington D.C., USA, Sept. 12-14, 2010.* 2010. p. 10.

Mahaffy, J. 2010. Development of Best Practice Guidelines for CFD in Nuclear Reactor Safety. *Nuclear Engineering & Technology, Vol. 42, No. 4.* 2010.

Menter, F. R. 1998-2002. *CFD Best Practice Guidelines for CFD Code Validation for Reactor Safety Applications, Evaluation of Computational Fluid Dynamic Methods for Reactor Safety Analysis (ECORA).* s.l. : European Commission, 5th EURATOM FRAMEWORK PROGRAMME, 1998-2002.

OECD/NEA. 2011. *MATiS-H Benchmark - Final Benchmark Specifications, pp. 44.* 2011.

Song, C.-H. and Lee, J. R. 2012. *OECD/NEA-KAERI Rod Bundle CFD Benchmark Exercise on Turbulent Mixing in a Rod Bundle with Spacers (MATiS-H) - Status Report on Experiments.* s.l. : Open Meeting for CFD Benchmark Exercise, OECD/NEA Headquarter, 30. May 2012, Paris, France, 2012.

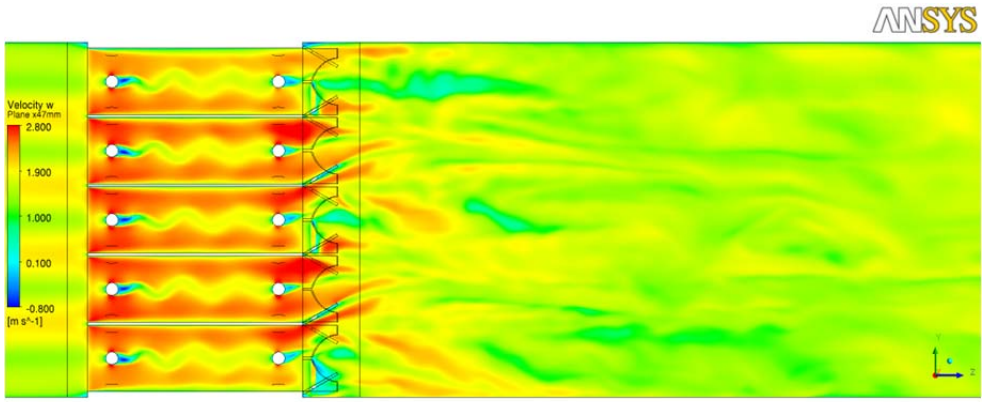

a) ANSYS CFX, SST-CC, Mesh3

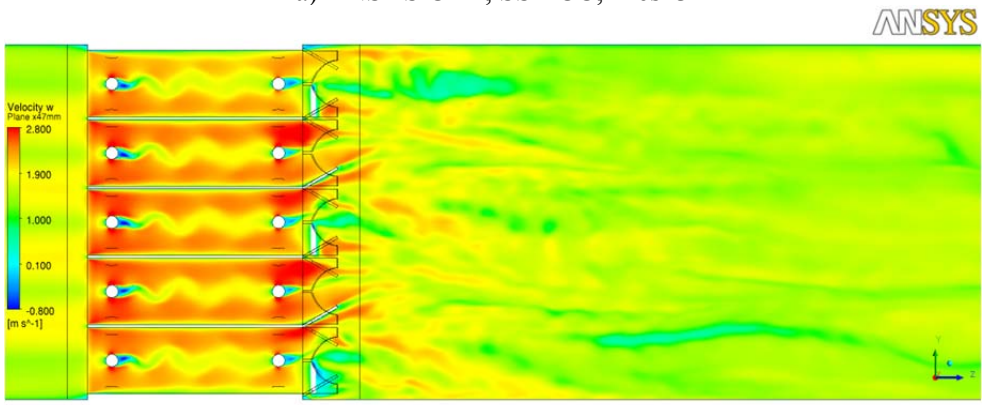

b) ANSYS CFX, BSLRSM, Mesh3

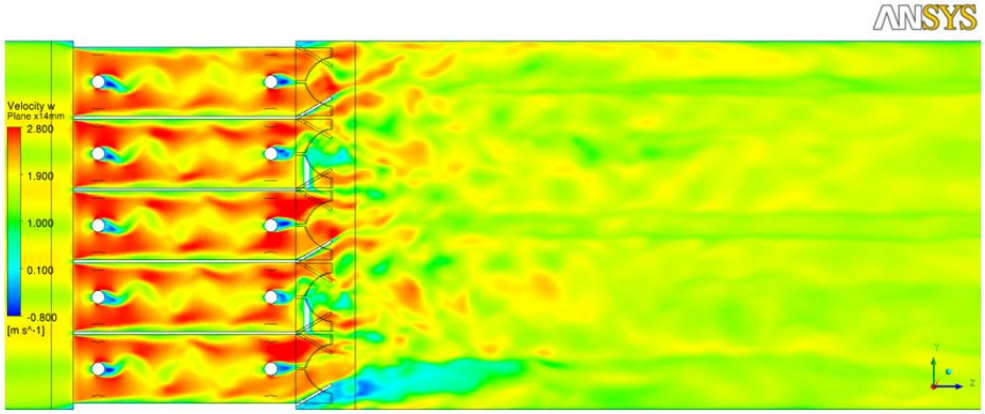

c) ANSYS Fluent, SST-CC, Mesh3

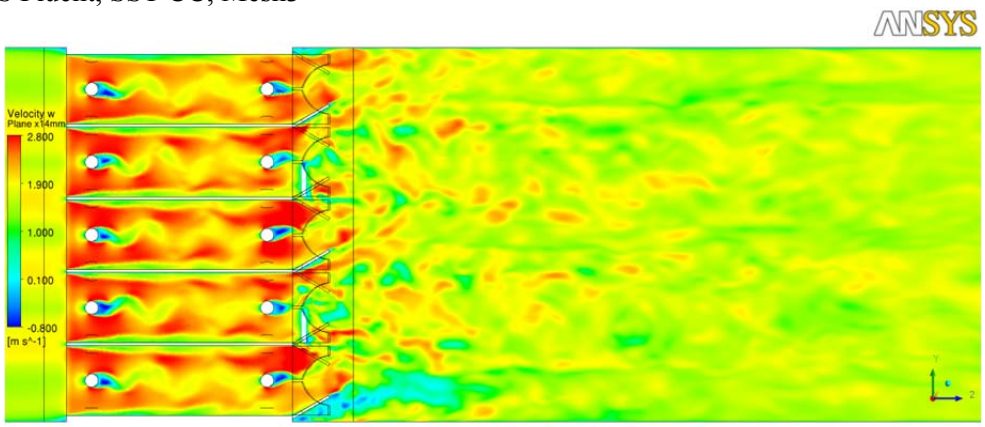

d) ANSYS Fluent, ω-RSM, Mesh3

Figure 6.3: Contours of instantaneous axial velocity component w in yz-plane cross section at x=0.014m; comparison of CFD solvers and turbulence model approaches.

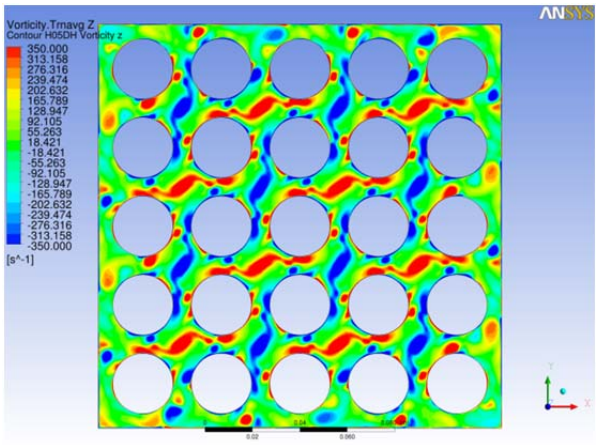

a) ANSYS CFX, SST-CC, Mesh3

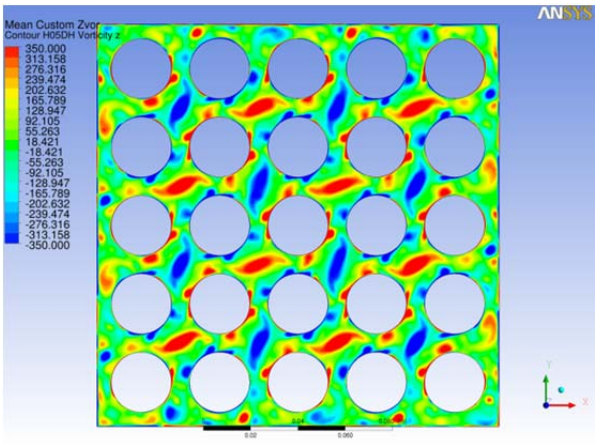

d) ANSYS Fluent, SST-CC, Mesh3

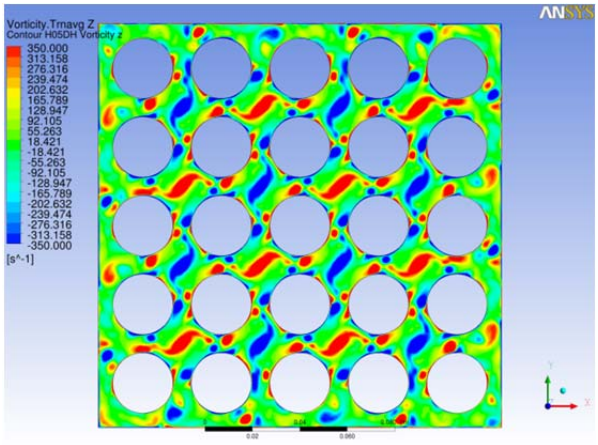

b) ANSYS CFX, BSLRSM, Mesh3

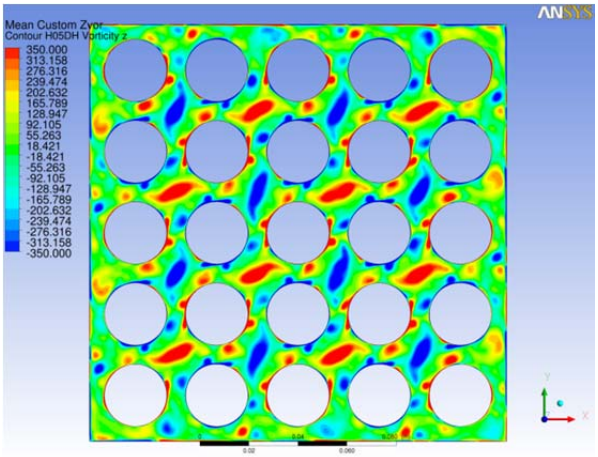

e) ANSYS Fluent, ω-RSM, Mesh3

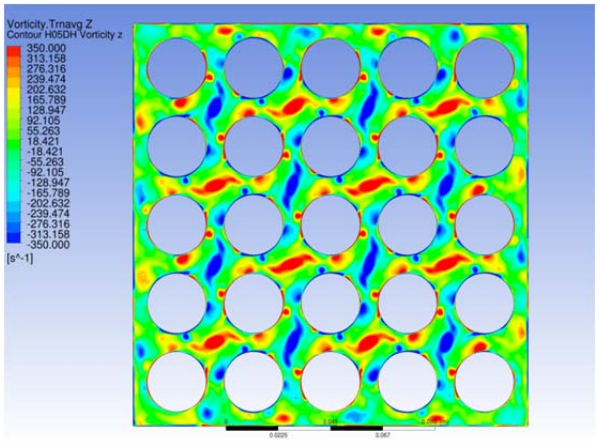

c) ANSYS CFX, ZLES SAS-SST, Mesh3

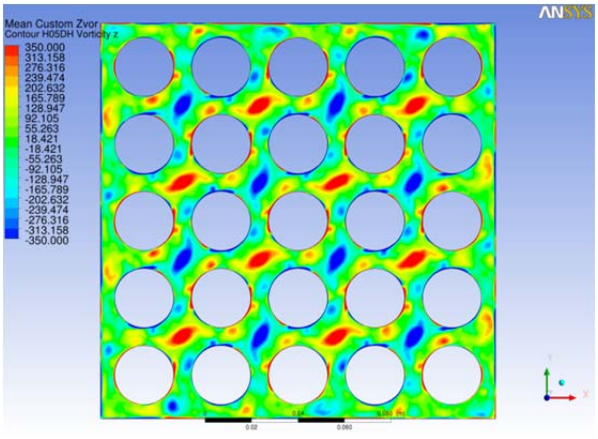

f) ANSYS Fluent, SAS-SST, Mesh3

Figure 6.4: Contours of time-averaged z-component of vorticity at xy-plane cross section at $z=0.5D_H$ downstream of the split type spacer grid.

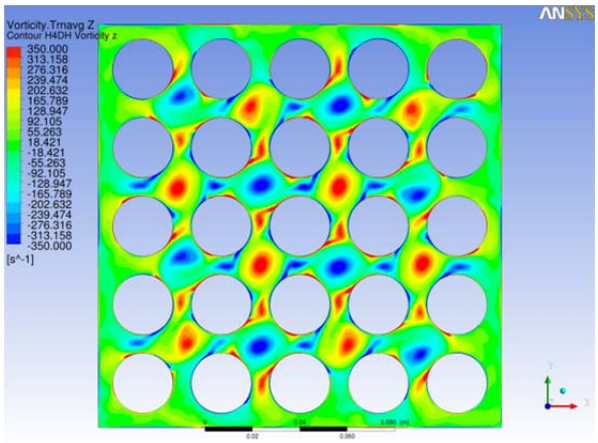

a) ANSYS CFX, SST-CC, Mesh3

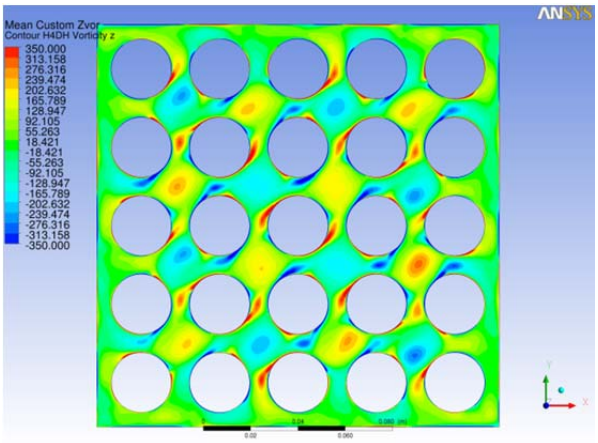

d) ANSYS Fluent, SST-CC, Mesh3

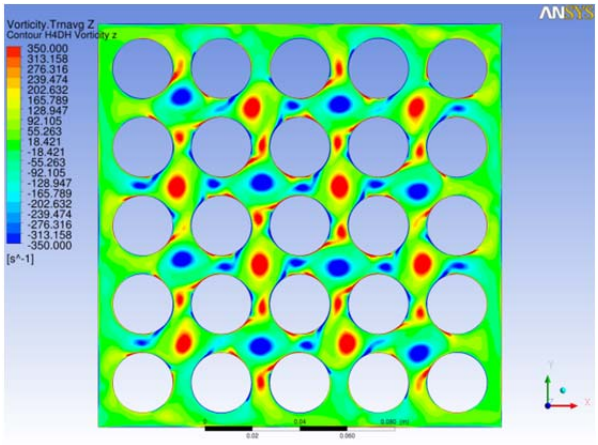

b) ANSYS CFX, BSLRSM, Mesh3

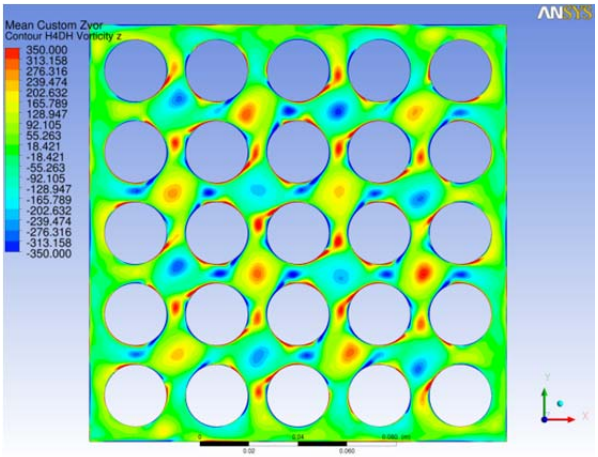

e) ANSYS Fluent, ω-RSM, Mesh3

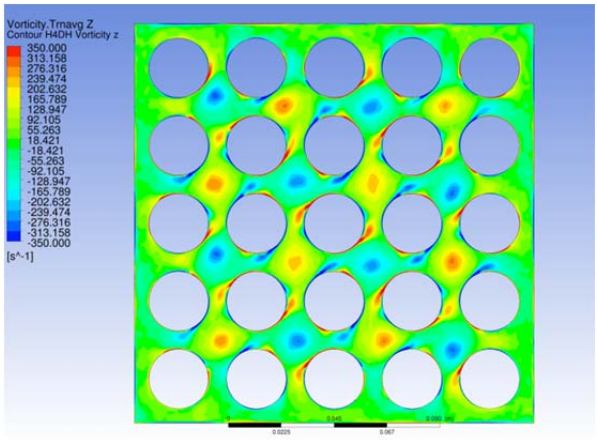

c) ANSYS CFX, ZLES SAS-SST, Mesh3

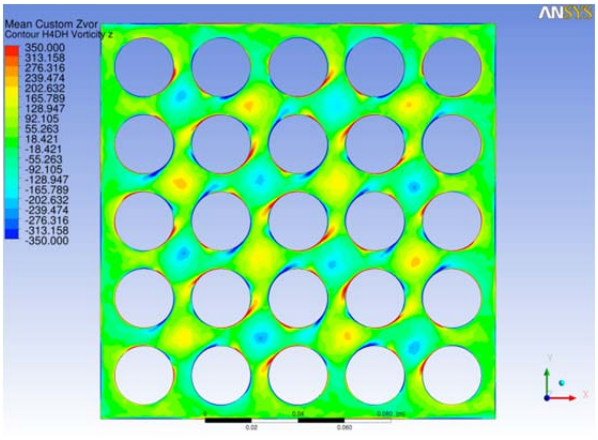

f) ANSYS Fluent, SAS-SST, Mesh3

Figure 6.5: Contours of time-averaged z-component of vorticity at xy-plane cross section at $z=4.0D_H$ downstream of the split type spacer grid.

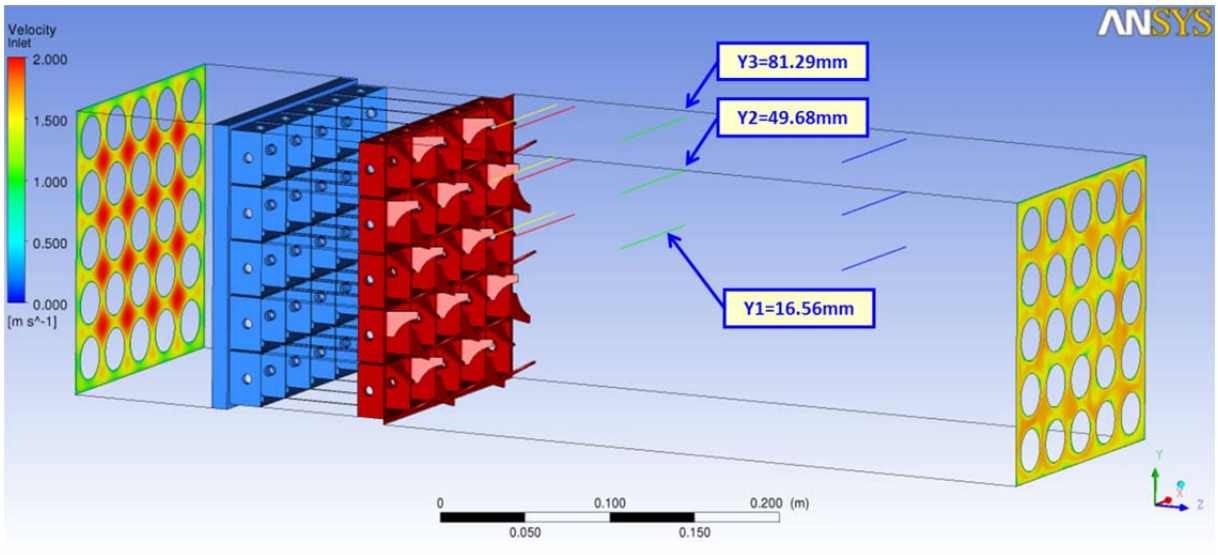

Figure 6.6: Location of line cross sections y1, y2 and y3 at different elevations z=0.5D_H, 1.0D_H, 4.0D_H and 10.0D_H in the MATiS-H rod bundle geometry with split type spacer grid.

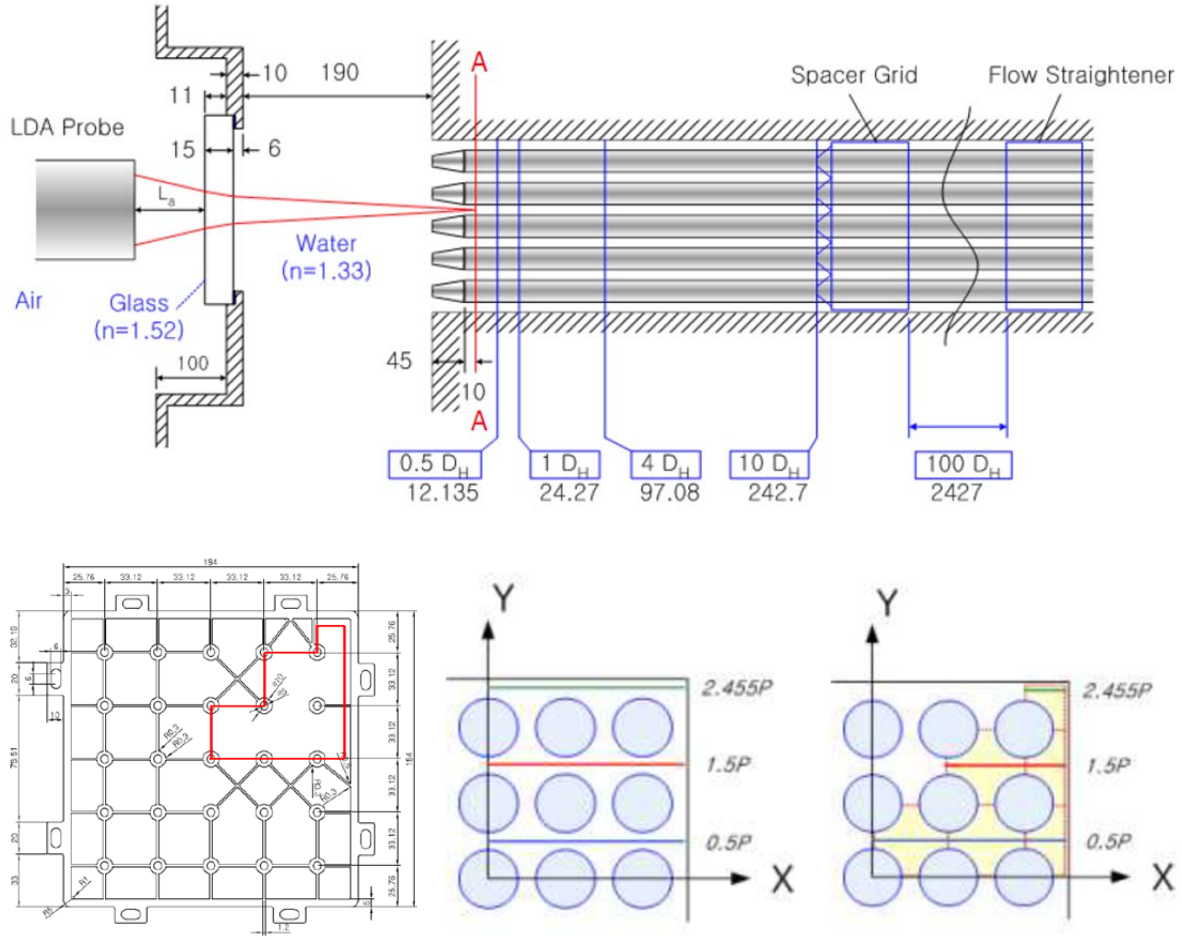

a) End support grid of the rod bundle b) Side measurement (w) c) Front measurement (u,v)

Figure 6.7: Optical configuration at KAERI MATiS-H test facility for front measurements. Location of measurement cross sections y1, y2 and y3 for different positions of the spacer grid at z=0.5D_H, 1.0D_H, 4.0D_H and 10.0D_H upstream the measurement plane in the MATiS-H rod bundle geometry.

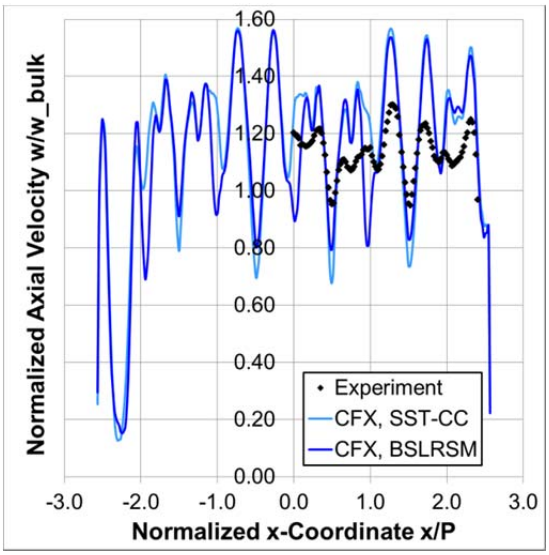

a) ANSYS CFX, Line y2, z=0.5D_H

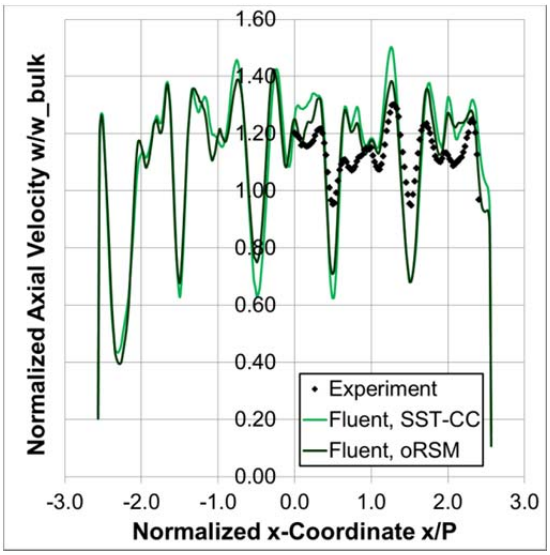

d) ANSYS Fluent, Line y2, z=0.5D_H

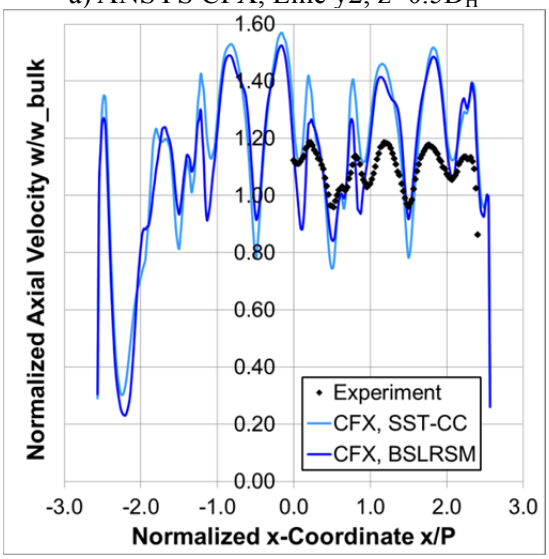

b) ANSYS CFX, Line y2, z=1.0D_H

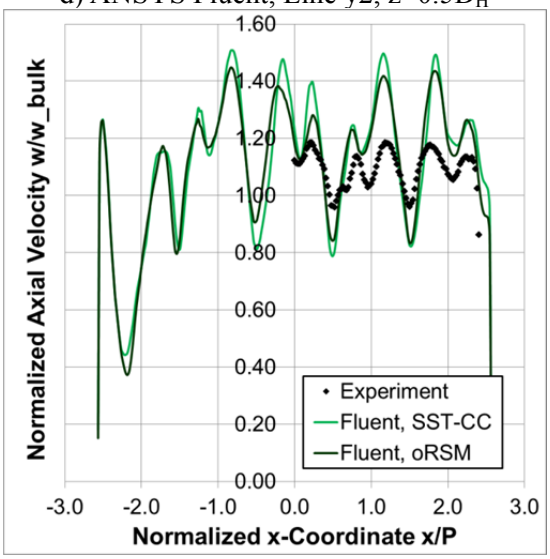

e) ANSYS Fluent, Line y2, z=1.0D_H

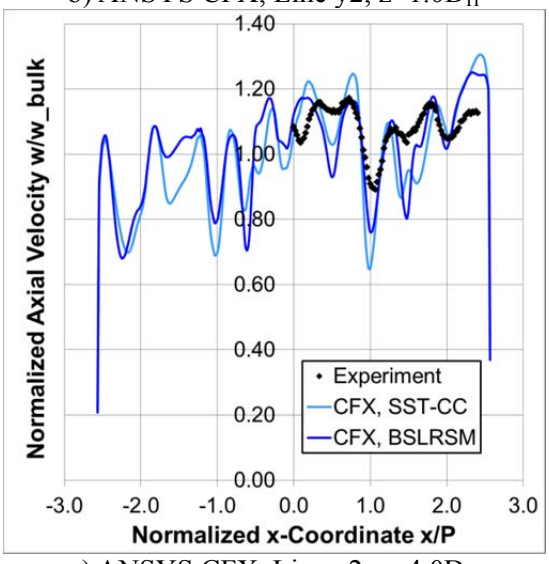

c) ANSYS CFX, Line y2, z=4.0D_H

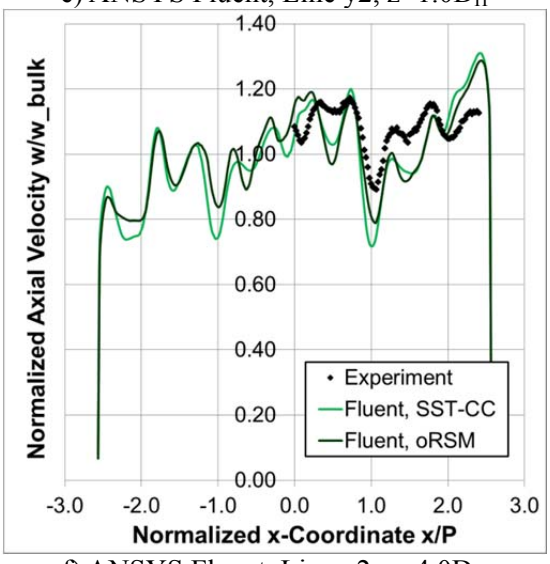

f) ANSYS Fluent, Line y2, z=4.0D_H

Figure 6.8: Comparison of time-averaged axial velocity component w for CFD solutions on Mesh3 at line y2=49.68mm for axial distances to the spacer grid at z=0.5D_H, z=1.0D_H and z=4.0D_H.

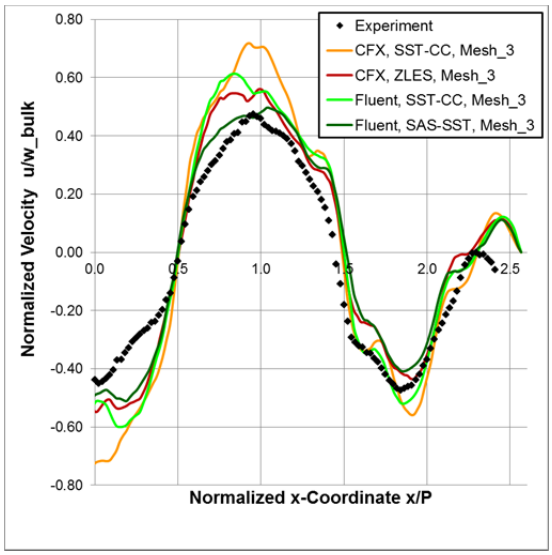

a) U velocity component, Line y1, z=0.5D_H

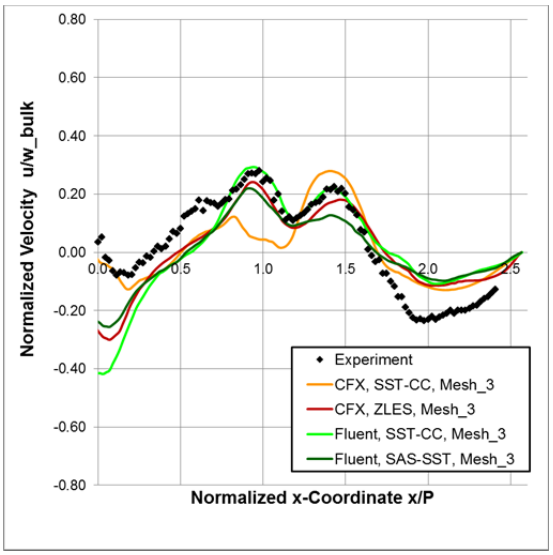

d) U velocity component, Line y1, z=4.0D_H

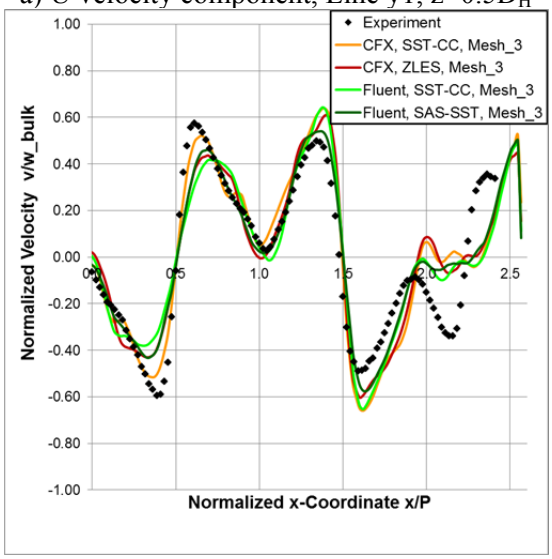

b) V velocity component, Line y1, z=0.5D_H

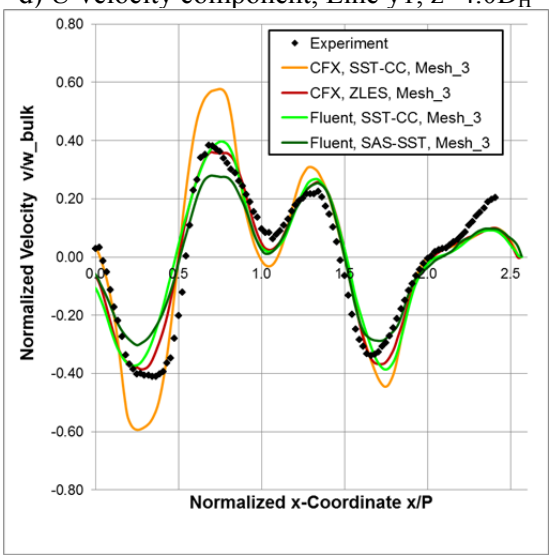

e) V velocity component, Line y1, z=4.0D_H

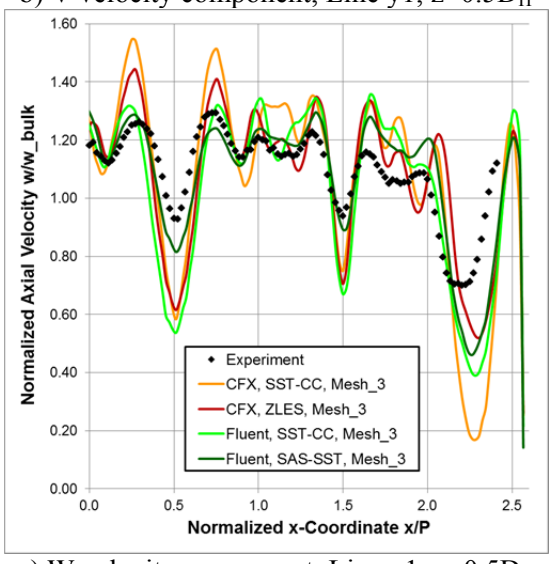

c) W velocity component, Line y1, z=0.5D_H

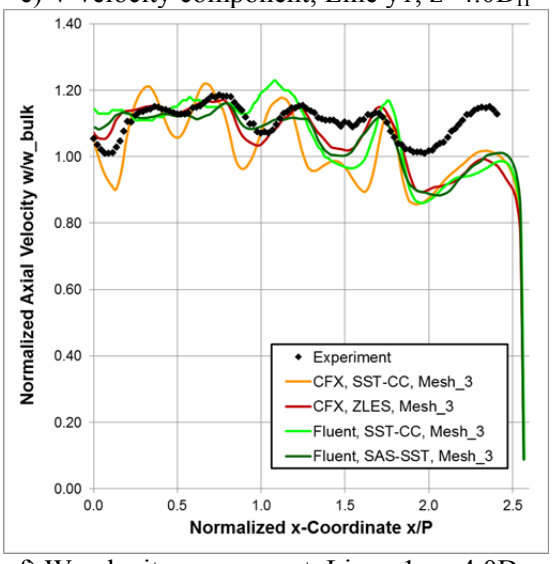

f) W velocity component, Line y1, z=4.0D_H

Figure 6.9: Results of SST model with curvature correction, SAS-SST (ANSYS Fluent) and ZLES SAS-SST (ANSYS CFX) on Mesh 3 for split type spacer grid. Comparison of time-averaged velocity components at line y1=16.56mm for axial distances to the spacer grid at z=0.5D_H and z=4.0D_H.

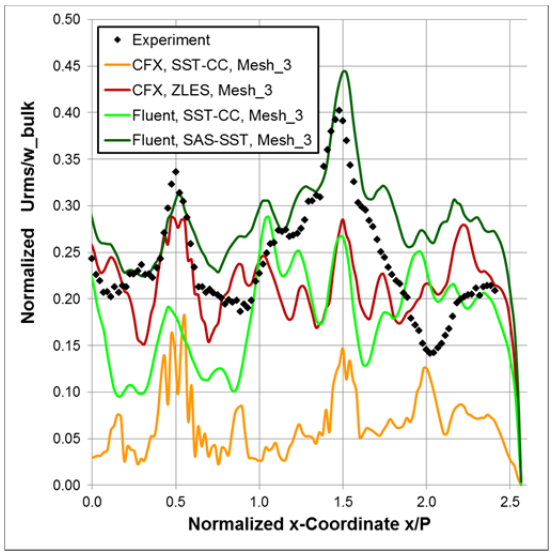

a) U_{RMS}, Line y1, z=0.5D_H

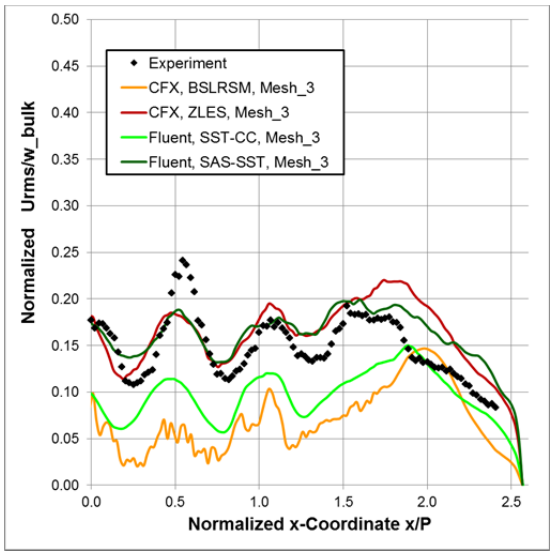

d) U_{RMS}, Line y1, z=4.0D_H

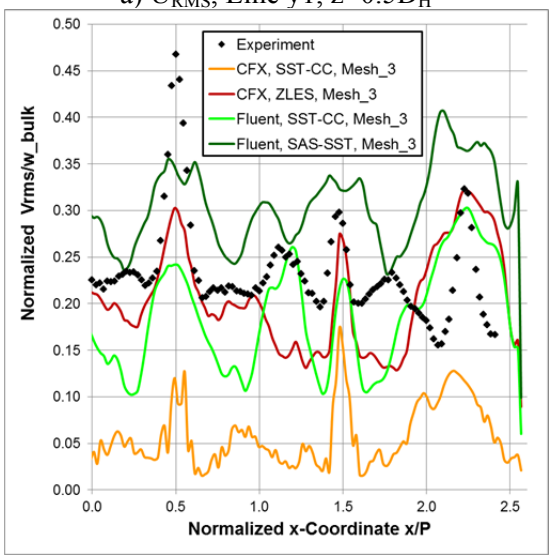

b) V_{RMS}, Line y1, z=0.5D_H

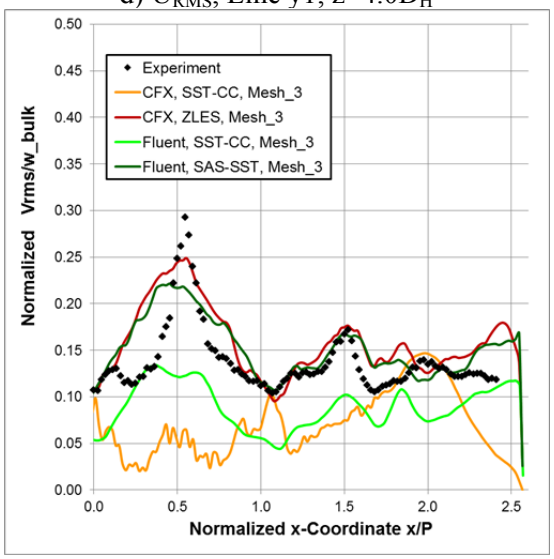

e) V_{RMS}, Line y1, z=4.0D_H

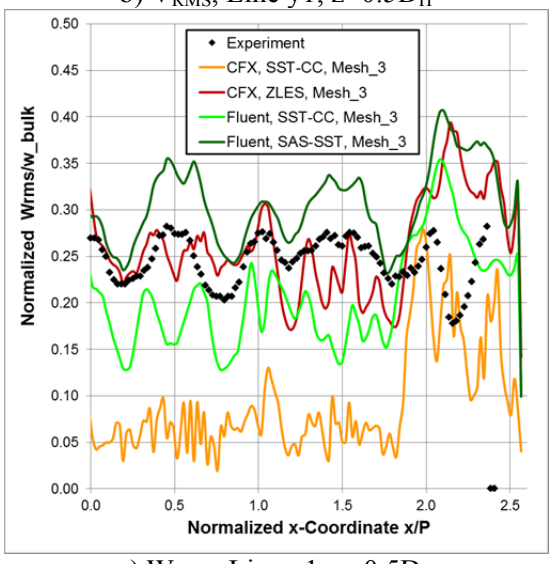

c) W_{RMS}, Line y1, z=0.5D_H

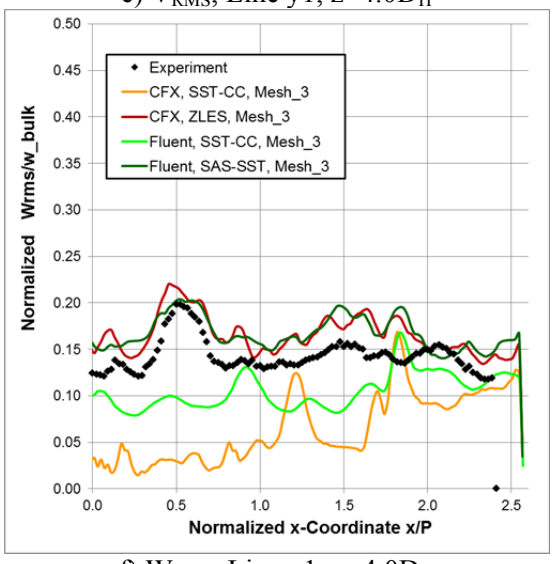

f) W_{RMS}, Line y1, z=4.0D_H

Figure 6.10: Results of SST model with curvature correction, SAS-SST (ANSYS Fluent) and ZLES SAS-SST (ANSYS CFX) on Mesh 3 for split type spacer grid. Comparison of time-averaged RMS values of velocity components at line y1=16.56mm for axial distances to the spacer grid at z=0.5D_H and z=4.0D_H.

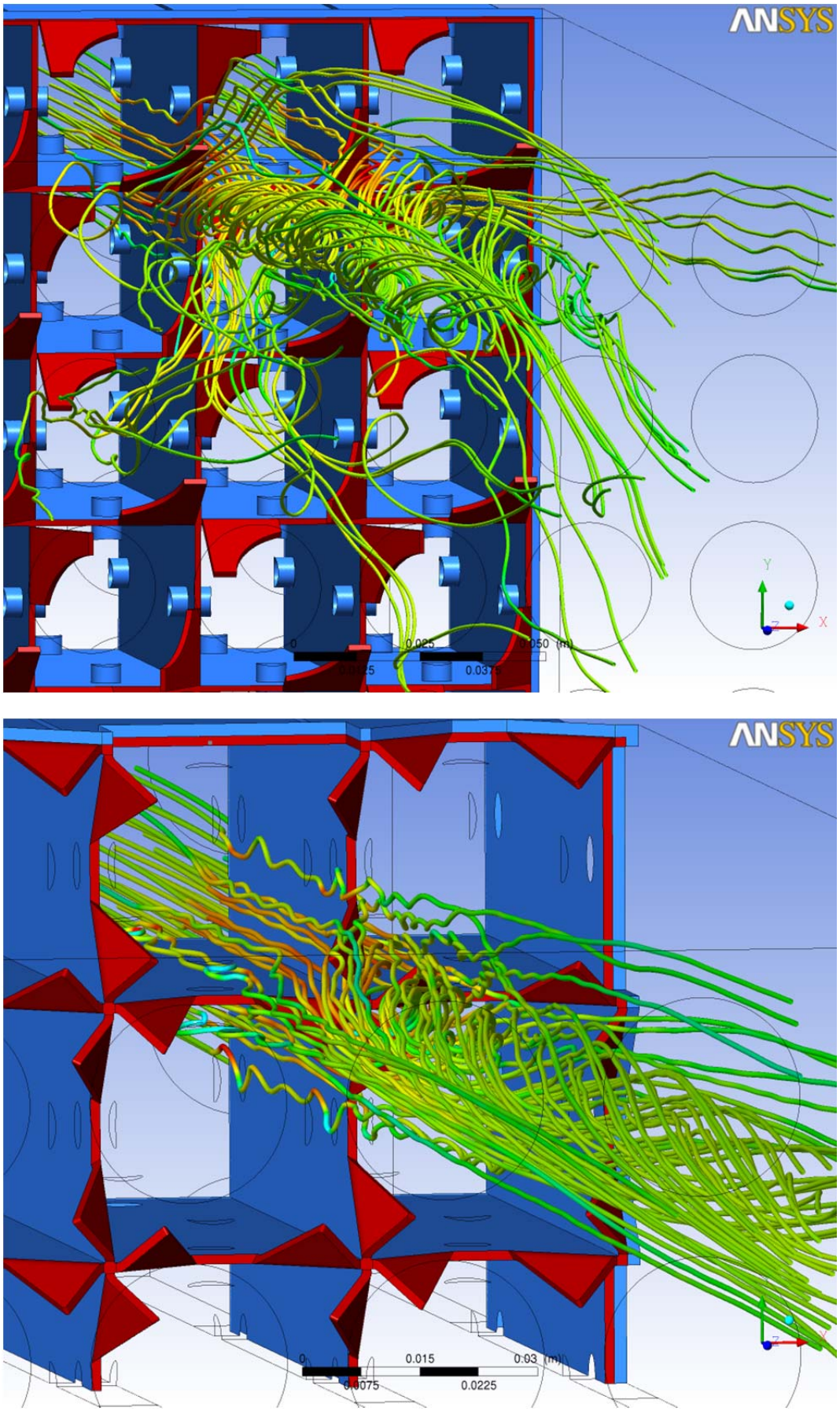

Figure 7.2: Streamlines in the 5×5 rod bundle with split and swirl type spacer grid geometry.

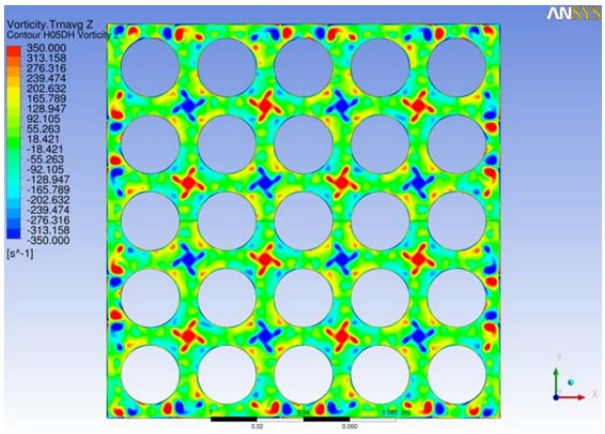

a) ANSYS CFX, BSLRSM, $z=0.5D_H$

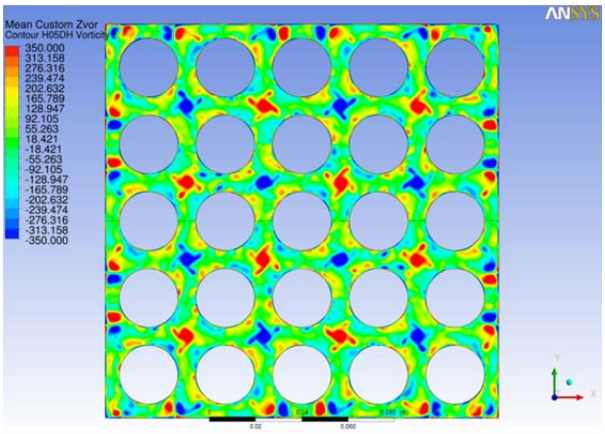

b) ANSYS Fluent, SST-CC, $z=0.5D_H$

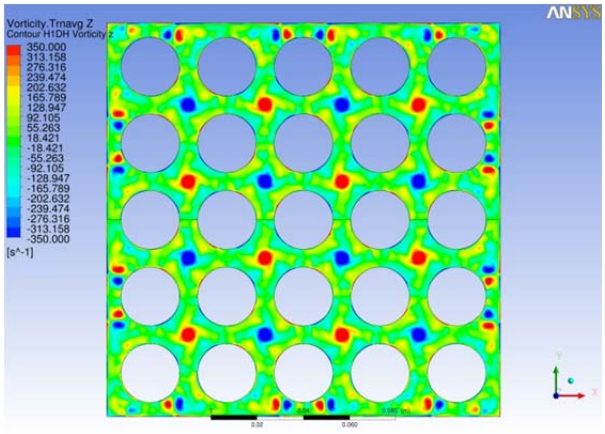

c) ANSYS CFX, BSLRSM, $z=1.0D_H$

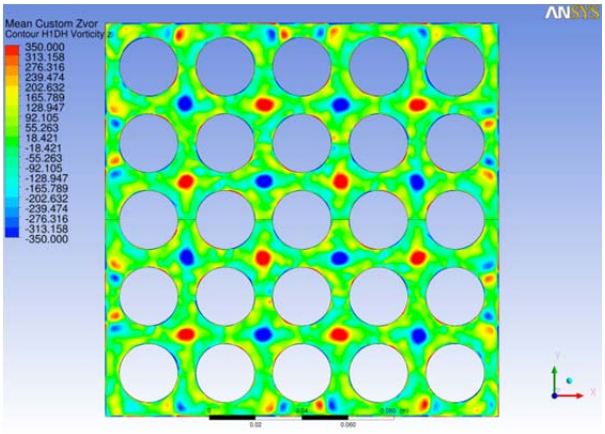

d) ANSYS Fluent, SST-CC, $z=1.0D_H$

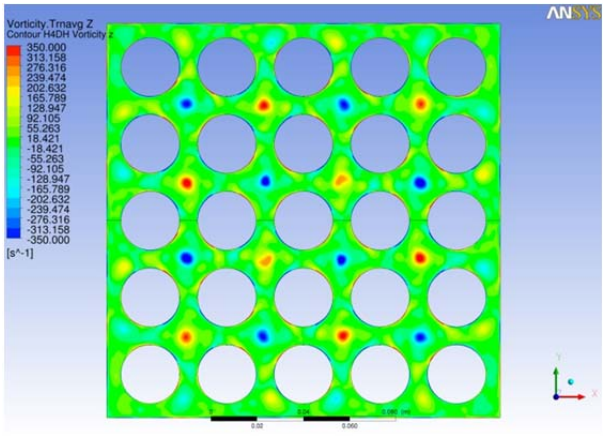

e) ANSYS CFX, BSLRSM, $z=4.0D_H$

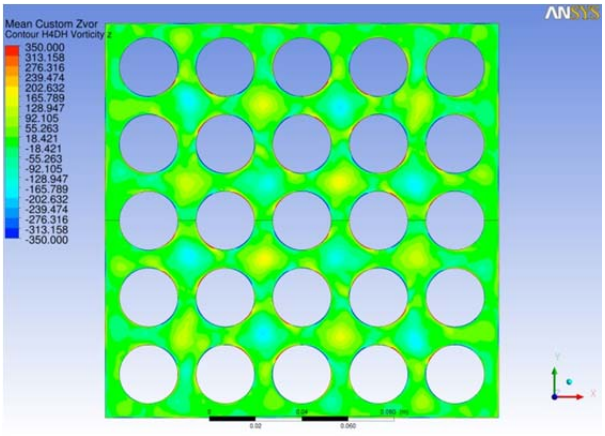

f) ANSYS Fluent, SST-CC, $z=4.0D_H$

Figure 7.3: Contours of time-averaged z-component of vorticity from URANS simulations at xy-plane cross sections at $z=0.5D_H$, $z=1.0D_H$, and $z=4.0D_H$ downstream of the swirl type spacer grid.

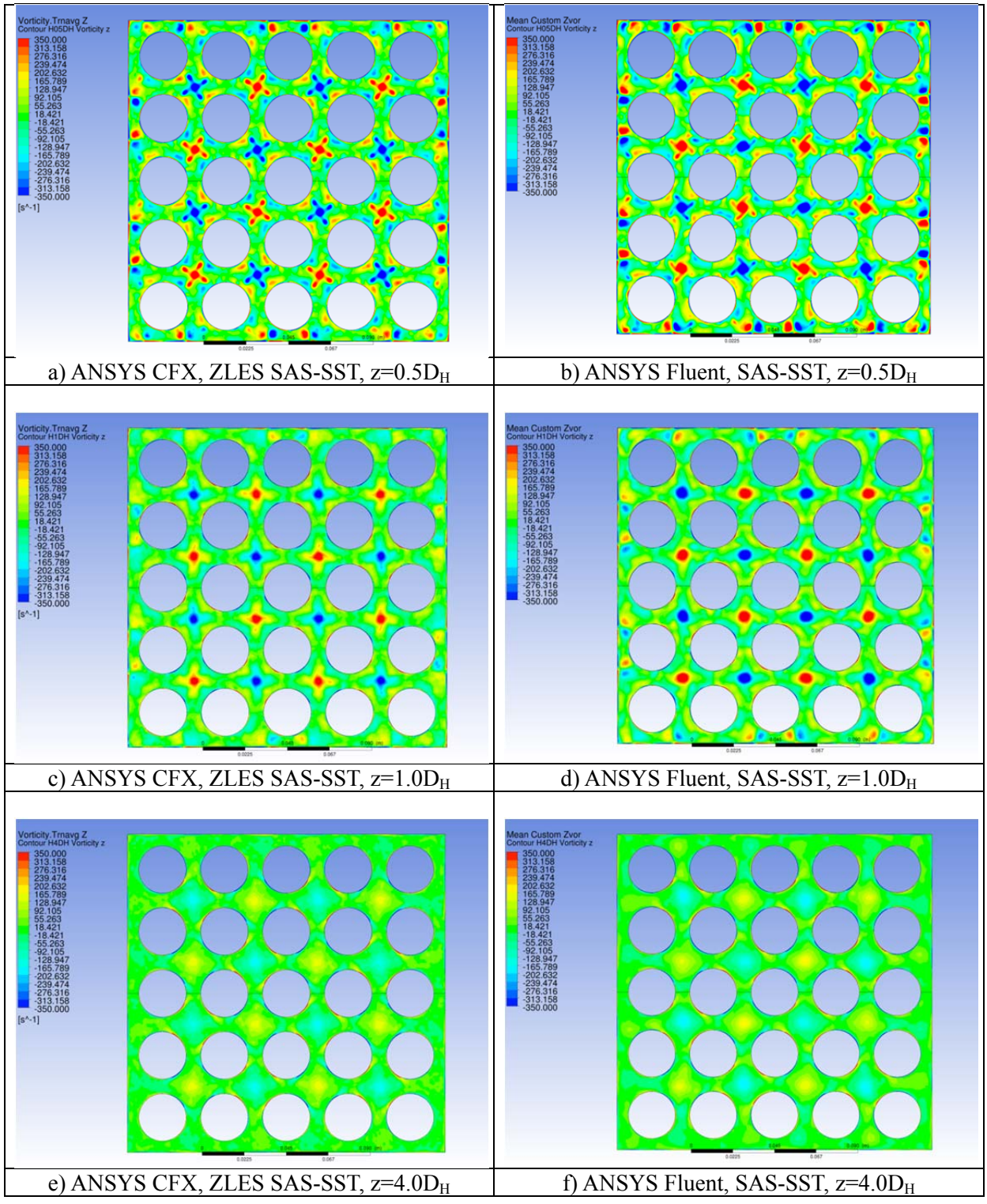

a) ANSYS CFX, ZLES SAS-SST, z=0.5D_H | b) ANSYS Fluent, SAS-SST, z=0.5D_H

c) ANSYS CFX, ZLES SAS-SST, z=1.0D_H | d) ANSYS Fluent, SAS-SST, z=1.0D_H

e) ANSYS CFX, ZLES SAS-SST, z=4.0D_H | f) ANSYS Fluent, SAS-SST, z=4.0D_H

Figure 7.4: Contours of time-averaged z-component of vorticity from SAS-SST simulations at xy-plane cross sections at z=0.5D_H, z=1.0D_H, and z=4.0D_H downstream of the swirl type spacer grid.

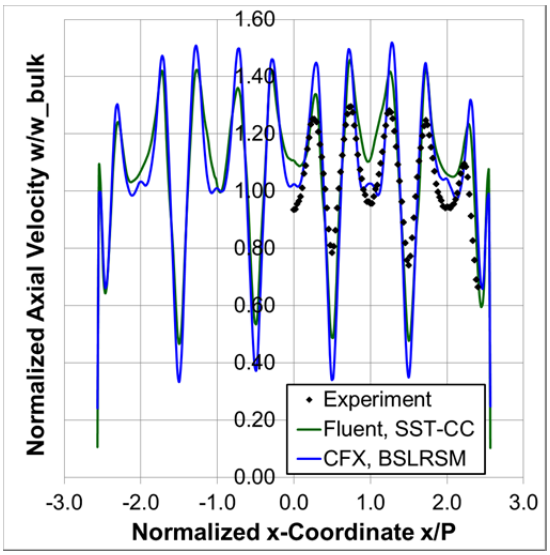

a) Line y1, z=0.5D_H

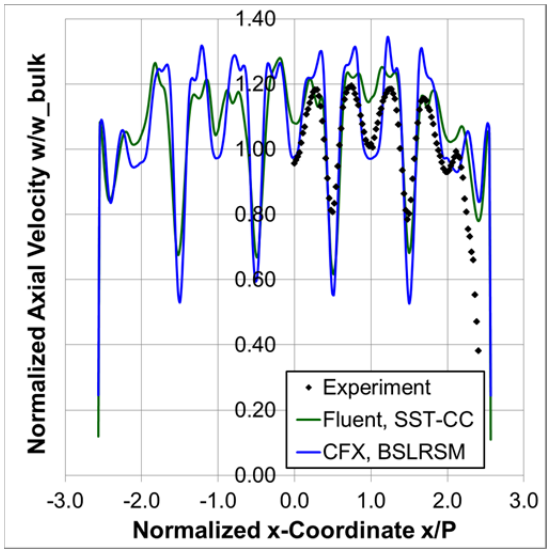

b) Line y1, z=1.0D_H

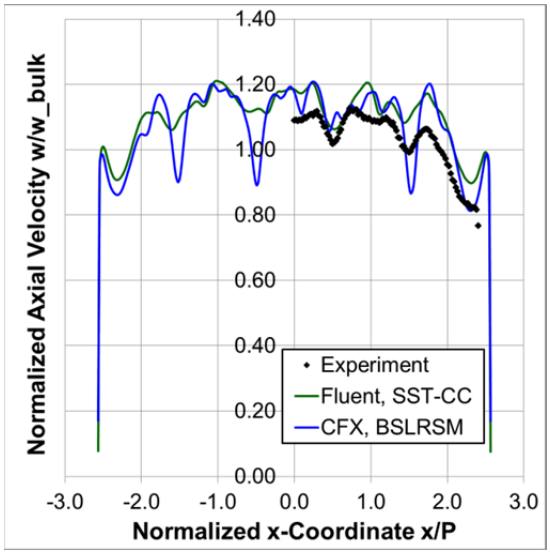

c) Line y1, z=4.0D_H

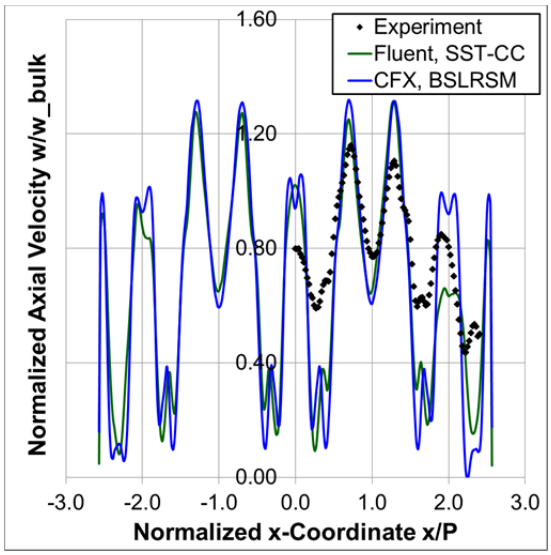

d) Line y3, z=0.5D_H

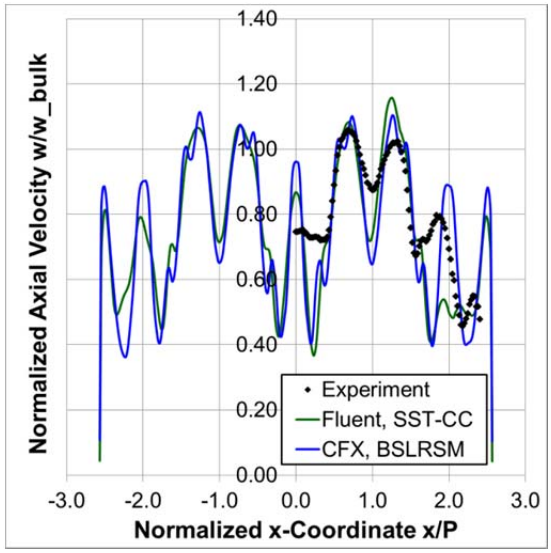

e) Line y3, z=1.0D_H

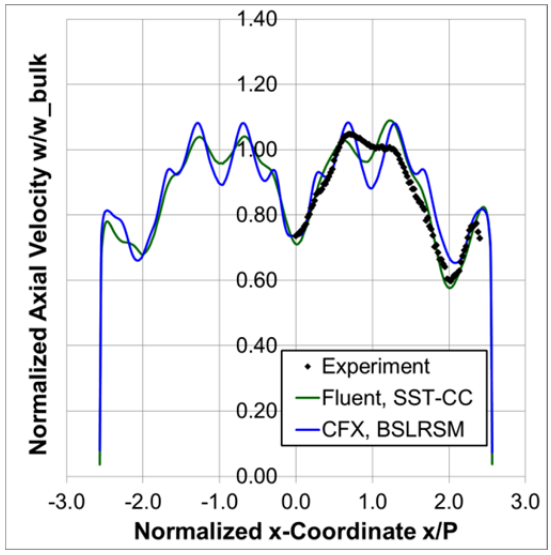

f) Line y3, z=4.0D_H

Figure 7.5: Comparison of time-averaged axial velocity component w at lines y1=16.56mm and y3=81.29mm for axial distances to the swirl type spacer grid at z=0.5D_H, z=1.0D_H and z=4.0D_H.

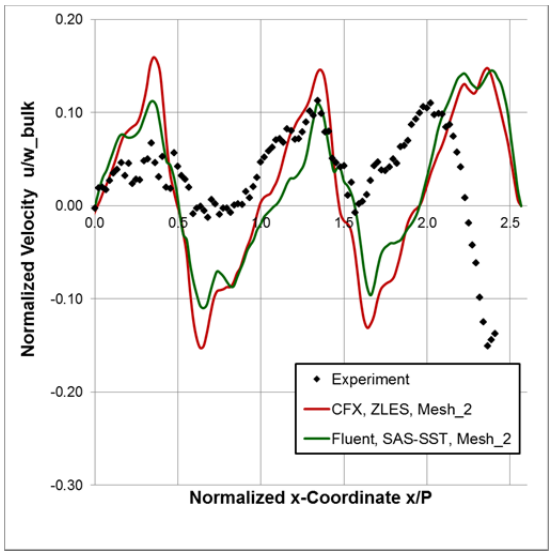

a) U velocity component, Line y1, z=0.5D_H

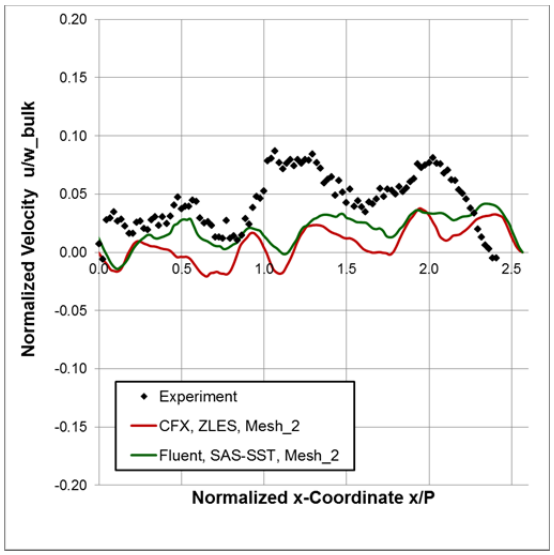

d) U velocity component, Line y1, z=4.0D_H

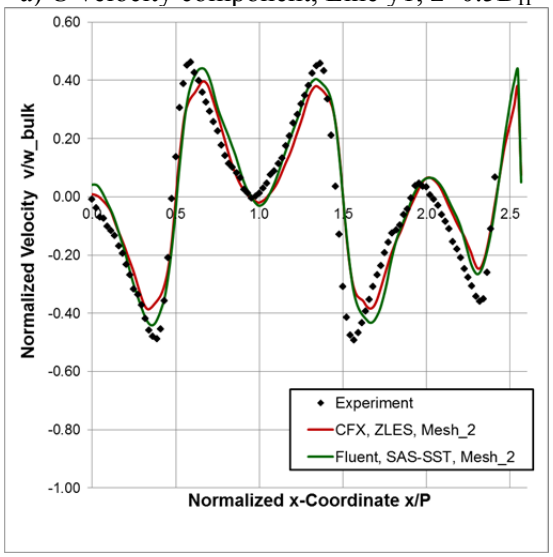

b) V velocity component, Line y1, z=0.5D_H

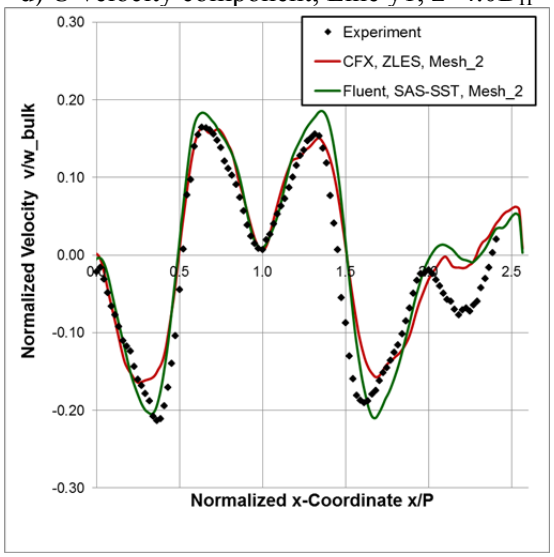

e) V velocity component, Line y1, z=4.0D_H

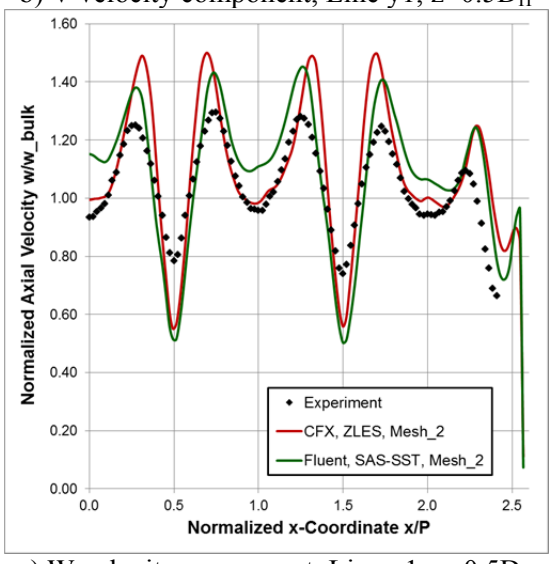

c) W velocity component, Line y1, z=0.5D_H

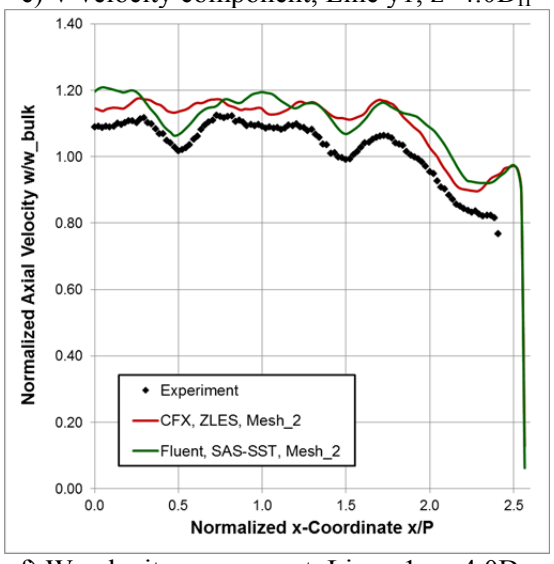

f) W velocity component, Line y1, z=4.0D_H

Figure 7.6: Results of SAS-SST (ANSYS Fluent) and ZLES SAS-SST (ANSYS CFX) on Mesh 2 for swirl type spacer grid. Comparison of time-averaged velocity components at line y1=16.56mm for axial distances to the spacer grid at z=0.5D_H and z=4.0D_H.

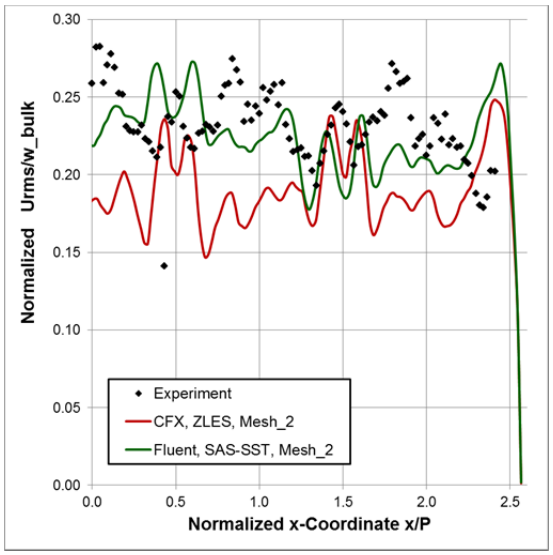

a) U_{RMS}, Line y1, z=0.5D_H

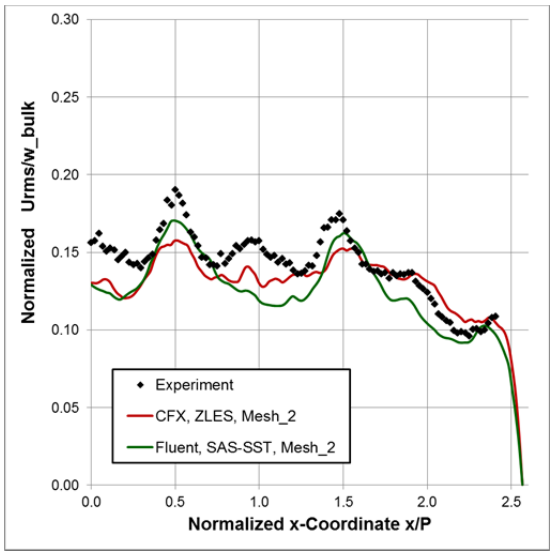

d) U_{RMS}, Line y1, z=4.0D_H

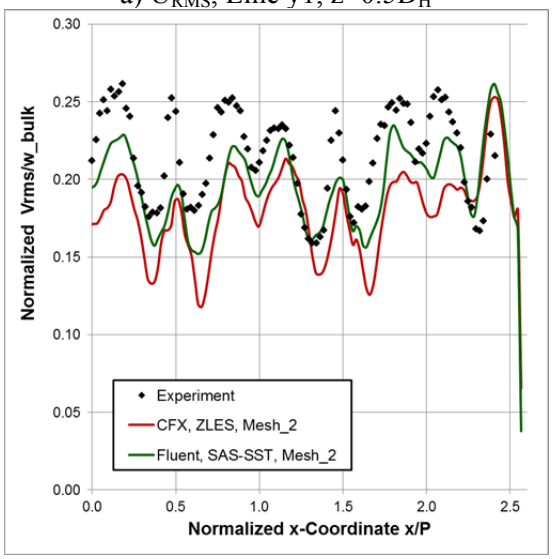

b) V_{RMS}, Line y1, z=0.5D_H

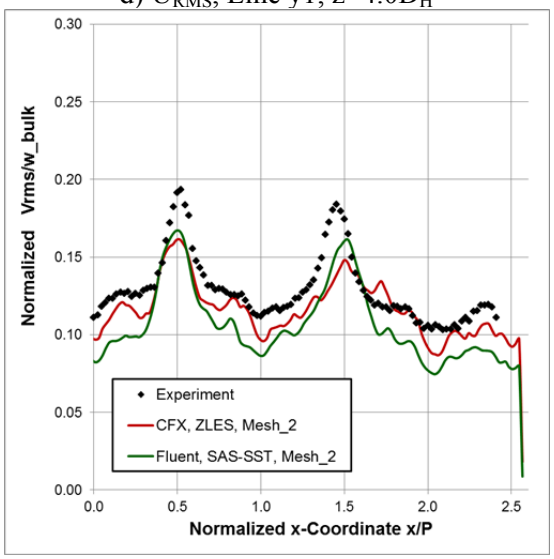

e) V_{RMS}, Line y1, z=4.0D_H

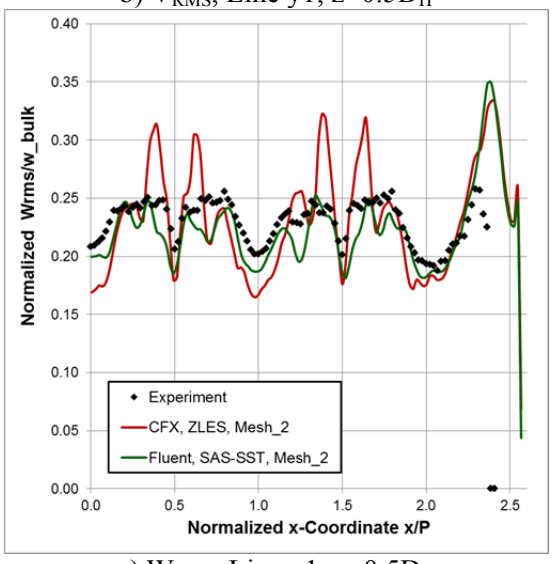

c) W_{RMS}, Line y1, z=0.5D_H

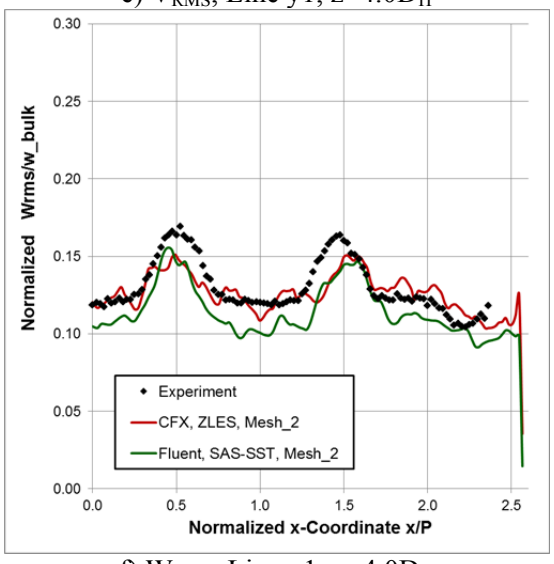

f) W_{RMS}, Line y1, z=4.0D_H

Figure 7.7: Results of SAS-SST (ANSYS Fluent) and ZLES SAS-SST (ANSYS CFX) on Mesh 2 for swirl type spacer grid. Comparison of time-averaged RMS values of velocity components at line y1=16.56mm for axial distances to the spacer grid at z=0.5D_H and z=4.0D_H.